Copyrighted Materials
Copyright © 2010 SciTech Publishing Retrieved from www.knovel.com

CHAPTER 5

Characteristics of Clutter

Nicholas C. Currie

Chapter Outline

5.1 INTRODUCTION AND DEFINITIONS

5.1.1 What Is Clutter?

Radar clutter is a radar return from an object or objects that is of no interest to the radar mission. For example, the mission of many radar systems is the detection and tracking of "targets" such as aircraft, ships, or ground vehicles. To these systems, clutter is considered to be an interfering return from a natural object such as precipitation, vegetation, soil and rocks, or the sea. However, to radars designed for remote sensing such as synthetic aperture radar (SAR) imagers, these objects may be the primary targets of interest. For this chapter, it will be assumed that targets of interest are man-made while natural target returns are unwanted (i.e., clutter).

5.1.2 Comparison of Clutter and Noise

Chapter 3 introduced detection in the presence of random noise, including noise properties and the effect on detection of targets. The returns from natural clutter can be strikingly similar to the effects of noise on detection yet also be quite different. So, how do clutter returns differ from noise effects? Figure 5-1 shows a high (fine) resolution (1 ft $\times$ 1 ft), two-dimensional (2-D) SAR image of a suburban terrain scene near Stockbridge, New York, collected from an airborne platform [1]. As can be seen from the figure, some areas appear uniform in nature (e.g., grassy lawns), while others appear quite nonuniform (e.g., trees and man-made structures). The high-resolution image shown in Figure 5-1 produces significantly different clutter properties from a lower-resolution radar, which averages out much of the structure shown in the figure. As an introductory text, this chapter will discuss the characteristics of lower-resolution (real-beam) systems.

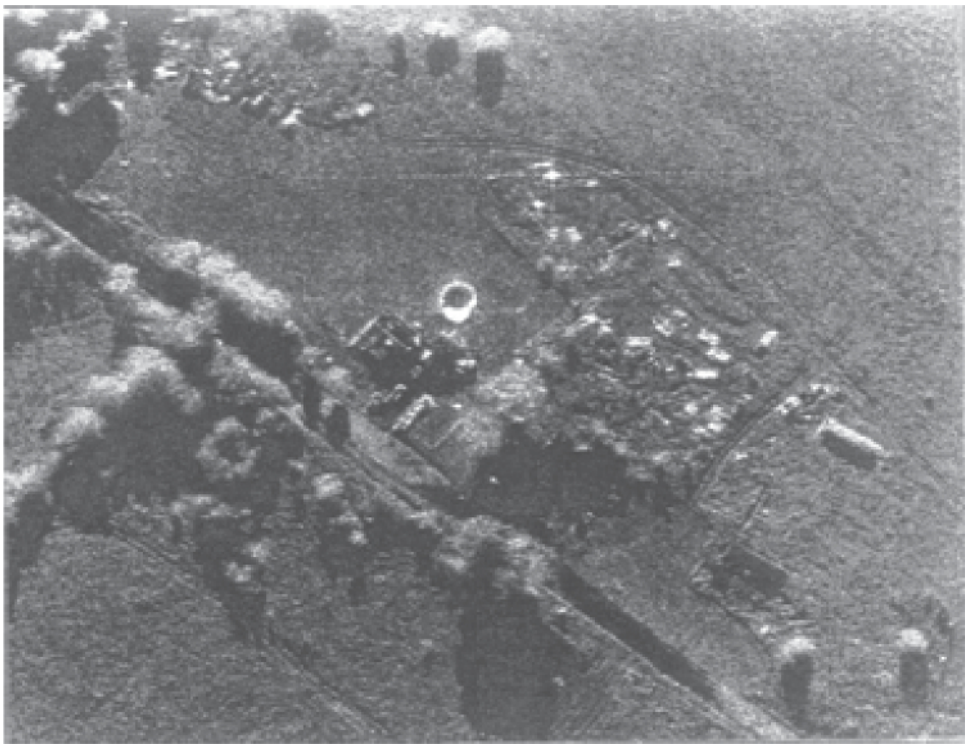

FIGURE 5-1 ■ Synthetic aperture radar image of suburban terrain. (From Novak and Owirka [1]. With permission.)

Table 5-1 summarizes the primary differences between clutter returns and receiver noise. Random noise, although varying with time, exhibits a specific set of characteristics:

- The probability density function (PDF) is Rayleigh for a linearly detected (voltage) signal, or exponential[1] for a square law detected (power) signal (see Chapter 3 for a description of the Rayleigh and exponential PDFs).
- The width of the autocorrelation function (ACF) is approximately the inverse of the receiver bandwidth.
- The power spectral density (PSD) function (power spectrum) width is approximately equal to the receiver bandwidth.

Clutter statistics can be similar to those of noise when the natural targets are composed of small, nearly equal-sized scatterers but can be quite different when the nature of the scatterers change or scatterers of differing types (e.g., a tree line) are present in the radar field of view. For this case, amplitude distributions having much longer "tails" than the Rayleigh distribution have been observed. Finally, although noise is independent of transmitted frequency, spatial position, and environmental parameters, clutter varies with all of these parameters, making clutter characterization very complex.

[1]The exponential PDF is sometimes called a *Rayleigh power* PDF. Confusingly, this is sometimes shortened to just Rayleigh PDF, even though the mathematical form intended is the exponential PDF. The Rayleigh PDF describes the amplitude (magnitude) of the noise signal; the magnitude squared (power) is described by an exponential PDF.

TABLE 5-1 ■ Clutter Signals versus Noise

Noise Signal	Clutter Signal
Amplitude independent of transmitted radar signal level	Amplitude proportional to transmitted radar signal level
Wide bandwidth (limited by receiver noise bandwidth)	Narrow bandwidth (created by scatterer motion)
Statistically independent between pulses	May be highly correlated between pulses
Amplitude variation described by Rayleigh statistics	Amplitude variation may vary from none to extremely wide (log normal or Weibull statistics)
Average value is constant and independent of spatial position	Time average will differ between spatial samples as the clutter types change
Independent of transmitted frequency	Varies with changing frequency
Independent of environmental parameters	Can vary with changing environmental conditions
No spatial component	Varies with beam position and resolution

Source: Adapted from Long [2]. (© 2006 IEEE. Used with permission.)

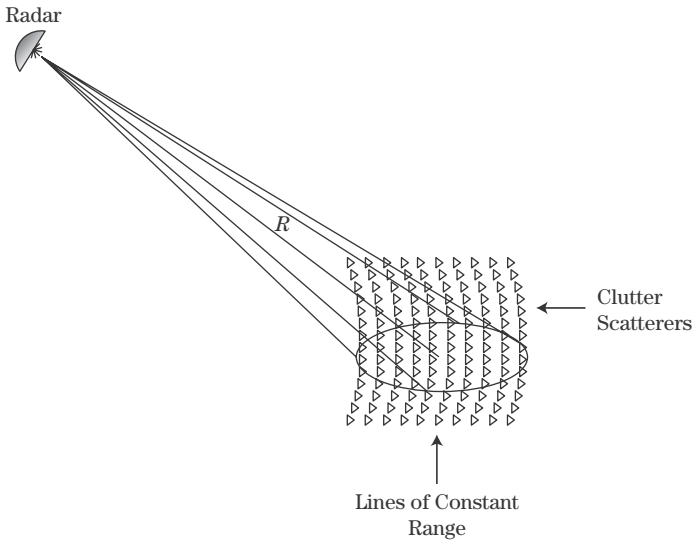

FIGURE 5-2 ■ Radar scan over clutter scatterers illustrating lines of constant range.

Figure 5-2 shows a typical situation where the radar beam illuminates a number of scatterers, each having a different reflectivity, σ_i, and distance, d_i, from the radar. Lines of constant range to the radar form ellipses on a level surface. The electric field amplitude (horizontal or vertical polarization component) measured at the radar due to the echo from the i-th scatterer will be proportional to the square root of the received power given by the radar range equation

$$|\boldsymbol{E}_i| = \left[\frac{P_t G^2 \lambda^2 \sigma_i}{(4\pi)^3 L_s d_i^4}\right]^{1/2} = k\frac{\sqrt{\sigma_i}}{d_i^2} \tag{5.1}$$

where P_t is the transmitted power, G is the antenna gain, λ is the wavelength, and L_s is the system loss (including hardware and atmospheric losses) as discussed in Chapter 2. The constant, k, absorbs all the factors that are the same for each scatterer. The phase of

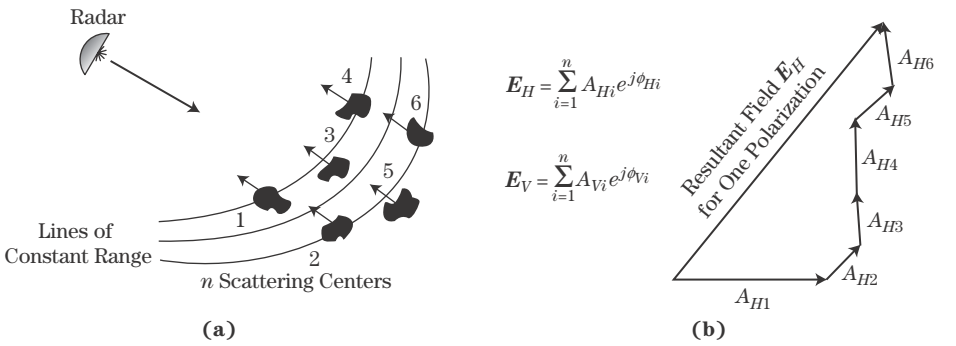

FIGURE 5-3 ■ Vector summation of scatterers at different positions and ranges. (a) Geometry of multiple scatterers. (b) Vector summation forms resultant E-field amplitude.

the received electric field, relative to the phase of the transmitted wave, is determined by the scatterer reflection phase, θ_i, and the two-way propagation distance:

$$\arg\{\boldsymbol{E}_i\} = \theta_i - \frac{4\pi}{\lambda} d_i = \theta_i + \phi_i \tag{5.2}$$

Scatterers located at the same range will generate echoes that return with the same time delay and phase at the radar, assuming that each scatterer has the same reflection phase (i.e., $\theta_i = \theta$) for some constant, θ. However, scatterers with slightly different ranges but falling within the same beam or range bin interval will have different echo phases. As shown in Figure 5-3a, the total return $\boldsymbol{E}$-field amplitude at the radar is therefore proportional to the vector summation of the electric field amplitude and phase of each group of scatterers contributing to a single radar measurement. This resultant $\boldsymbol{E}$-field is given by

$$\begin{aligned} \boldsymbol{E} &= \sum_i \boldsymbol{E}_i = \sum_i k \frac{\sqrt{\sigma_i}}{d_i^2} \exp\left[-j\left(\frac{4\pi}{\lambda} d_i + \theta_I\right)\right] \\ &\approx \frac{k}{d^2} \sum_i \sqrt{\sigma_i} \exp\left[-j\left(\frac{4\pi}{\lambda} d_i + \theta_I\right)\right] \\ &\equiv \frac{k'}{d^2} \sqrt{\sigma} \exp[j\phi] \end{aligned} \tag{5.3}$$

where d is the nominal range to the resolution cell and σ is the equivalent radar cross section (RCS) of the total clutter return, and ϕ is the equivalent phase. This process is illustrated in Figure 5-3b. The complex quantity $\sqrt{\sigma}\exp[j\phi]$ is called the *backscatter coefficient* of the clutter.

As the radar beam scans across the scatterers in the scene, the range to the particular scatterers in the beam changes so that the resulting equivalent RCS changes. This variation in return has come to be known as "speckle": the "noise-like" returns resulting from the random summation of individual scatterer echoes. The reduction of this characteristic, "despeckling," is very important in SAR processing. As the beam scans farther, new scatterers enter the beam, while other scatterers leave the beam. For a mechanically scanned system, the changes are smooth, while for an electronic scan system the changes occur abruptly as the beam is step-scanned. As long as the scatterers illuminated at any given time are similar in amplitude and phase, the return will exhibit noise-like statistics with constant parameters. However, if the beam scans across a set of scatterers that are physically different the character of the return can change. An example is scanning from a grassy field to a line of trees, which would likely result in an increase in the echo strength and thus the equivalent RCS. Also, the presence of one or two large scatterers among the smaller scatterers can cause the return to exhibit very nonnoise-like statistics.

Since the returns from clutter vary by type, polarization, environmental, and geometric conditions, it is very difficult to model clutter mathematically. Attempts to do so are briefly discussed in Section 5.3. More practically, many experiments have been conducted to measure clutter returns as functions of the various dependent parameters. Practical clutter modeling usually involves a combination of empirical and theoretical results.

5.1.3 Basic Definitions

5.1.3.1 Scattering Coefficients

To use published data on clutter, methods must be defined to normalize the returns so that data can be applied to many different radars and applications. One form of the radar equation can be written as

$$P_r = \frac{P_t G^2 \lambda^2 \sigma}{(4\pi)^3 L_s R^4} \tag{5.4}$$

where the variables are the same as in equation (5.1). This form of the radar equation is suitable for point targets (i.e., targets much smaller than the resolution of the radar) but is not convenient for distributed targets such as clutter, where many scatterers contribute at once to the total echo. Thus, equation (5.4) must be modified to account for the area or volume defined by the beamwidths and range resolution of the radar.

For surface clutter it is convenient to define the radar cross section per unit area, or *surface reflectivity*,

$$\sigma^0 \equiv \frac{\sigma}{A} \tag{5.5}$$

where σ is the total RCS of the contributing clutter, and A is the area of the contributing clutter defined by the radar beam intersection with the surface. The units of σ^0 are meters^2/meters^{2}so that σ^0 is unitless. It is often expressed in the literature in decibels, denoted dBsm/sm.

For volume clutter, the radar cross section per unit volume, or *volume reflectivity,* is defined as

$$\eta = \frac{\sigma}{V} \tag{5.6}$$

where V is the volume defined by the radar beam and range resolution cell. The units of η are meters^2/meters^3, or meter^{-1}. It is expressed in the literature in decibels per meter.

Given σ^0, the area A to be used in computing clutter RCS using equation (5.5) for surface clutter is determined by the beamwidths and the range resolution of the radar. Two situations arise: (1) the case where the range resolution is large compared with the projection of the vertical beam width onto the surface; and (2) the case where the range resolution is smaller than the projection extent. In the *beam-limited* case, the result for the beam area on the ground was

$$A = \pi R^2 \tan\left(\frac{\theta_3}{2}\right) \tan\left(\frac{\phi_3}{2}\right) \csc\delta \tag{5.7}$$

where ϕ_3 and θ_3 are the azimuth and elevation beamwidths of the antenna, respectively, and δ is the *grazing angle* of the antenna boresight with the clutter surface. For beamwidths less than about 10 degrees the small angle approximation $\tan(x) \approx x$ is valid, and

equation (5.7) becomes

$$A = \frac{\pi R^2}{4}\theta_3\phi_3 \csc\delta \tag{5.8}$$

Note that since the clutter area grows as R^2 due to beam spreading, so will the clutter RCS, σ. When used in equation (5.4), the resulting received power due to a constant clutter reflectivity will be proportional to R^{-2} instead of the R^{-4} proportionality seen for point targets. Thus, beam-limited surface clutter power does not decline with range as rapidly as does point target power.

In the *pulse-limited* case, the area defined by the beam and pulse width on the ground is given by

$$A = \left(\frac{c\tau}{2}\right) 2R\tan\left(\frac{\theta_3}{2}\right)\sec\delta = c\tau R\tan\left(\frac{\theta_3}{2}\right)\sec\delta \tag{5.9}$$

and, again, if the beam width is less than 10°, a small angle approximation gives

$$A = \left(\frac{c\tau R\theta_3}{2}\right)\sec\delta \tag{5.10}$$

Note that in this case the clutter area is proportional to R instead of R^2. Consequently, the pulse-limited echo power from constant-reflectivity surface clutter declines as R^{-3}. If the radar uses pulse compression techniques (see Chapter 20) to obtain fine-range resolution, then the radar range resolution in meters should replace the factor $c\tau/2$ in equations (5.9) and (5.10).

The grazing angle at which the clutter cell area transitions from the beam-limited case to the pulse-limited case can be found by setting the pulse- and beam-limited areas equal to one another and is given by

$$\tan\delta = \frac{\pi R\tan(\phi_3/2)}{c\tau} \tag{5.11}$$

or, for small antenna beamwidths,

$$\tan\delta = \frac{\pi R\phi_3}{2c\tau} \tag{5.12}$$

When the value of $\tan\delta$ exceeds the value in equations (5.11) or (5.12), the beam-limited case applies. Conversely, when $\tan\delta$ is less than that value, the pulse-limited case applies.

Note that the beamwidths used in the previous equations are assumed to be the 3 dB two-way beamwidths. Actual radar beams are not rectangular, so some errors can occur in beam area and clutter power estimation based on the actual beam shape and sidelobes. These errors can be significant for airborne pulse-Doppler processors.

The previous discussion can be applied to area clutter (e.g., ground, sea). For computing the equivalent RCS of atmospheric clutter using equation (5.6), the reflectivity, η, and the resolution cell volume, V, defined by the radar beam and the pulse width are needed. Since air search radars are almost always narrow beam, the small angle approximation formula is usually adequate. This is given by

$$V = \pi\left(\frac{R\theta_3}{2}\right)\left(\frac{R\phi_3}{2}\right)\left(\frac{c\tau}{2}\right) = \left(\frac{\pi R^2\theta_3\phi_3}{4}\right)\left(\frac{c\tau}{2}\right) \tag{5.13}$$

Again, the actual range resolution should be used in place of the $(c\tau/2)$ term in pulse compression radars.

5.1.3.2 Clutter Polarization Scattering Matrix

The scattering properties of clutter are dependent on the transmitted and received polarization. This effect is quantified by the use of a 2-by-2 matrix known as the *polarization scattering matrix* (PSM), **S** [3]. Equation (5.14) gives a form of the matrix expressed in terms of vertical and horizontal polarization:

$$\mathbf{S} = \begin{bmatrix} \sqrt{\sigma_{HH}}\, e^{j\phi_{HH}} & \sqrt{\sigma_{HV}}\, e^{j\phi_{HV}} \\ \sqrt{\sigma_{VH}}\, e^{j\phi_{VH}} & \sqrt{\sigma_{VV}}\, e^{j\phi_{VV}} \end{bmatrix} \tag{5.14}$$

The first subscript represents the received polarization, while the second represents the transmitted polarization. For example, the lower left term in the matrix describes the vertically polarized received voltage signal component in response to a horizontally polarized transmitted signal. In fact, a matrix can be developed in terms of any two orthogonal polarizations, including circular and elliptical polarizations.

The terms in the complex matrix **S** represent the backscattering coefficients of the clutter for four polarization cases: (1) transmit and receive horizontal polarization; (2) transmit horizontal and receive vertical polarization; (3) transmit vertical and receive horizontal polarization; and (4) transmit and receive vertical polarization. For a specific frequency and geometry of the radar and a specific set of environmental parameters, the polarization scattering matrix contains all of the available information about the clutter return at the time of the measurement.

Unfortunately, a radar that can transmit and receive all four polarizations is both complex and expensive. Fortunately, for the case of a monostatic radar the *reciprocity theorem* [3] requires that the two "cross polarized" terms are equal, that is, $\sigma_{VH} = \sigma_{HV}$ and $\phi_{VH} = \phi_{HV}$. Thus, only three complex polarization values must be measured to determine the full scattering matrix.

Much work has been done to try to exploit the information inherent in the scattering matrix to identify targets in the presence of clutter. Holm [4] and others have attempted to use the scattering matrix to separate targets from clutter as well as to identify classes or types of targets on the theory that the PSMs of man-made targets and natural clutter will be significantly different. He determined that, to be effective, high-range and azimuthal resolution is required so that individual range-azimuth cells contain only target returns or only clutter returns. If cells contain a mixture of both target and clutter returns, the results are much less useful even if the clutter returns are much lower in amplitude than the targets.

In the past, attempts to use partial polarization matrix information to discriminate between targets and clutter have been tried with mixed results [3,5]. Such discriminants have included the following:

- Parallel/cross polarization ratio: $\sqrt{\sigma_{HH}}/\sqrt{\sigma_{VH}}$.
- Vertical/horizontal polarization ratio: $\sqrt{\sigma_{VV}}/\sqrt{\sigma_{HH}}$.
- Polarimetric phase: $\phi_{HH} - \phi_{VV} \equiv \phi_{H-V}$.

Polarimetric phase is usually expressed as quadrature components $\cos(\phi_{H-V})$ and $\sin(\phi_{H-V})$. These discriminants have the advantage of requiring only the polarimetric amplitude or phase instead of the entire PSM and can improve target detectability in clutter under some conditions.

5.2 GENERAL CHARACTERISTICS OF CLUTTER

5.2.1 Overview

Because clutter is one of the major limitations in target detection for practical radar, clutter measurements have been performed since the advent of radar use in World War II. The development of digital recording techniques has greatly improved the quality (and quantity) of data in the last 20 years. Because clutter exhibits noise-like fluctuations in echo strength, clutter is characterized in terms of statistical parameters describing the variability of σ^0 and η, including the following:

- Mean or median values.
- Standard deviations or variances.
- Probability density functions.
- Spectral bandwidths for temporal variability.
- Autocorrelation functions or power spectral density functions for temporal and spatial variations.

These measured values almost always include propagation factor effects (see Chapter 4). Usually, for clear air measurements of surface clutter at moderate to high angles the propagation factor effects are negligible. However, for measurements of atmospheric precipitation or for low grazing angles for surface clutter, attenuation due to multipath can be significant. These effects can be minimized by using calibration targets located near the clutter region being measured but can never be totally eliminated. For this reason, data from precipitation or surface clutter at large ranges tend to have more variability than measurements of surface clutter at steeper grazing angles. Since an operational radar will experience these same effects under the same conditions, this situation is not necessarily bad.

5.2.2 Surface Clutter

5.2.2.1 General Dependencies

Given that the radar-received clutter power in a particular application affects the detection performance and influences radar design, a simple and accurate way is needed to estimate clutter levels for a variety of scenarios. The goal is to develop models that include in a mathematical form all the known parameter dependencies of the backscattering coefficient that have been identified through experimental measurements. Fundamentally, clutter model development starts with theoretical calculations of reflectivity and comparison with the interpretation of experimental observations, which leads to an understanding of the underlying scattering mechanisms. Some of the observed dependencies are as follows:

- *Grazing angle*: Grazing angle, δ, is the angle at which the illumination energy strikes a clutter surface.
- *Vertical variation of the clutter scatterers*: Rough surfaces have a larger σ^0 than smooth ones for low grazing angles; at very high grazing angles (near 90°), smooth surfaces have a higher σ^0 than rough ones.
- *Wavelength*: σ^0 is a function of vertical texture expressed in wavelengths.

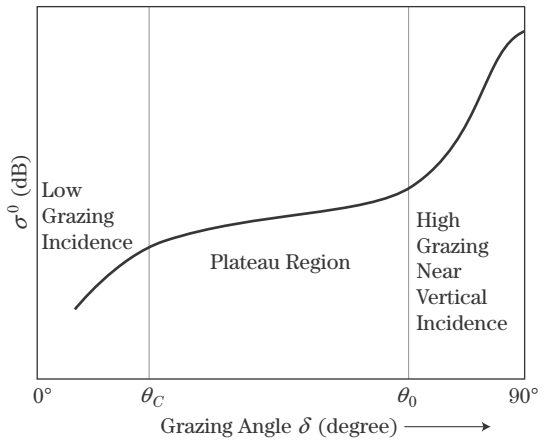

FIGURE 5-4 ■ General dependence of σ^0 on grazing angle. (Adapted from [6]. With permission.)

Depression angle is closely related to grazing angle. It is the angle below the radar's local horizontal at which the illumination energy is transmitted from the radar. For a flat horizontal clutter surface the depression and grazing angles are identical. Grazing angle is the most relevant for describing scattering, but clutter reflectivity data are often reported as a function of depression angle in the literature because the grazing angle may not be known precisely. In this chapter, the two are generally assumed to be the same unless otherwise stated, and the discussion is framed in terms of grazing angle. Depression angle is used when referring to previous published results given in terms of depression angle.

Rough surface theory and experimental measurements have determined that the backscattering for both land and sea surfaces—as a function of grazing angle—exhibit a common general dependence on grazing angle as shown in Figure 5-4. From this figure, three distinct regions of clutter behavior can be identified: (1) a low grazing angle region; (2) a plateau region; and (3) a high grazing angle region. The boundaries of these three regions, defined by θ_C and θ_0, change with frequency, surface condition, and polarization [6].

The *low grazing angle region* extends from zero to a *critical angle,* θ_C, determined by the root mean square (rms) height of surface irregularities in wavelengths. This critical angle is the grazing angle below which a surface seems "smooth" by Rayleigh's definition and above which it is "rough." Based on Rayleigh's definition, a surface is smooth if

$$\sigma_h \sin \delta < \frac{\lambda}{8} \tag{5.15}$$

where σ_h is the rms height of the surface irregularities, δ is the grazing angle, and λ is the radar wavelength. Thus, the critical angle is given by

$$\sin \delta_C = \frac{\lambda}{8\sigma_h} \tag{5.16}$$

In the *plateau region* the incident wave encounters the surface irregularities in such a way that the dependence of σ^0 on grazing angle is much less than at lower angles. Chapter 7 provides an introduction to the "rough surface" theory applicable to this regime.

For a constant σ^0 and beam-limited geometry, it is expected that the return power for surface clutter would vary as $R^{-4} \times R^2 = R^{-2}$ since the power from a point target varies as R^{-4} while the area of surface clutter increases as R^2. However, measurements have indicated that clutter power often varies as R^{-3}. For this to be the case, σ^0 must vary as

R^{-1}. The grazing angle satisfies the equation $\sin\delta = h/R$, where h is the radar altitude and R is the slant range. If the height of the radar is constant, then $\sin\delta$ is proportional to $1/R$. This fact led to the definition of the so-called *constant gamma model* for clutter reflectivity, given by

$$\sigma^0 = \gamma \sin\delta = \frac{\gamma}{R} \tag{5.17}$$

Here γ is a constant depending on terrain type, surface roughness (sea state and terrain type for sea and land, respectively), and frequency. If equation (5.17) applies, then clutter reflectivity will be proportional to R^{-1}, and the R^{-3} clutter power dependence would be expected. Note that the constant gamma model is applicable only in the plateau angular region.

In the *high grazing angle region* the scattering becomes more directional and rapidly increases to a maximum value based on the reflectivity and smoothness of the clutter, in a manner somewhat analogous to the behavior of the main lobe of a rough flat plate at near perpendicular incidence (see Chapter 6).

Figure 5-5 gives the RCS of a conducting sphere of diameter a normalized to its projected area as a function of the circumference normalized to the wavelength. As can be seen from the figure, the relative RCS increases with frequency, $2\pi/\lambda$, until λ equals twice the circumference, whereupon the RCS varies rapidly until λ is about $1/5$ the circumference, at which point the RCS equals the projected cross sectional area of the sphere and is independent of frequency. Thus, for large wavelengths (low frequencies), the return from a sphere would be expected to increase with increasing frequency until the point known as the *resonance region*, where the RCS fluctuates rapidly with frequency. Cylinders exhibit similar frequency dependence relative to the ratio of circumference to wavelength. Since most clutter scatterers can be considered to be approximately either spherical or cylindrical in shape, clutter RCS should be expected to increase with decreasing wavelength up to a wavelength in the millimeter wave region for most scatterers. At high frequencies facets or ripples create resonance effects that overcome this effect. As will be seen in the data, this effect does exist, although variations among different types of clutter return can often be much greater than frequency effects.

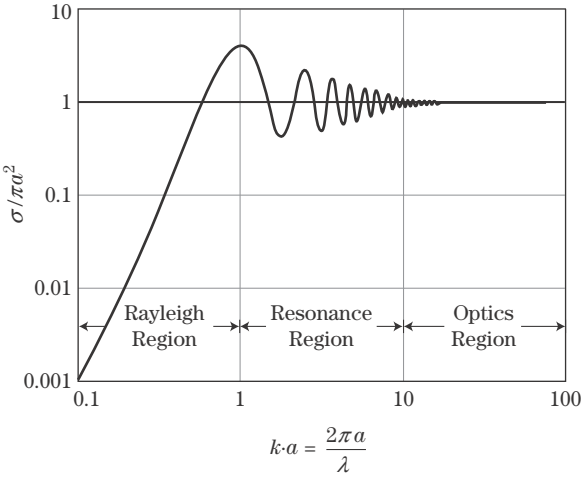

FIGURE 5-5 ■ Dependence of the RCS of a sphere on wavelength.

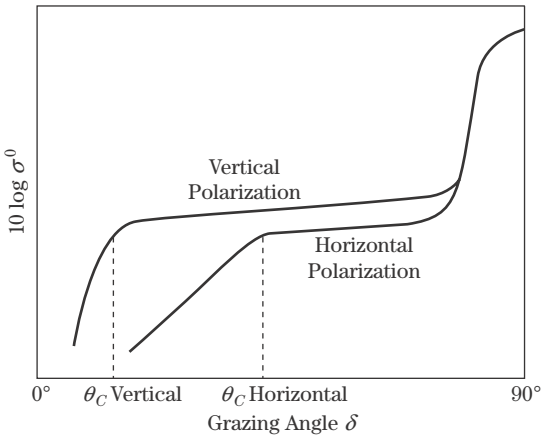

FIGURE 5-6 ■ Theoretical polarization dependence of a relatively smooth surface. (From Long [6]. With permission.)

Figure 5-6 gives the theoretical polarization dependence of σ^0 (generally verified by experiment) as a function of grazing angle for a moderately smooth surface, which tends to occur at lower frequencies. The critical angle, θ_C, occurs at different grazing angles for the two polarizations due to multipath effects so that at lower angles the difference between clutter reflectivity at vertical and horizontal polarizations can be quite large. However, for higher angles and frequencies, the horizontal polarization reflectivity is usually only a few dB lower than the vertical polarization reflectivity. Although these polarization trends on average are valid, for specific clutter patches the occasional presence of natural diplanes can result in widely varying polarization returns.

5.2.2.2 Temporal and Spatial Dependencies

Temporal and spatial variations occur due to either the motion of scatterers within the radar cell (usually due to wind) or the nature of scatterers changing as the radar cell moves in range or azimuth. Such statistical variation is described in terms of probability distributions with simple mathematical equations to facilitate modeling. Coherent receiver noise has a complex normal (Gaussian) amplitude distribution before detection and a Rayleigh distribution after detection, assuming a linear (voltage) detector, or an exponential distribution if a square law (power) detector is used. Clutter amplitudes can also appear Gaussian or Rayleigh distributed for the low-resolution case where there are a large number of scatterers within the radar cell. However, as the resolution improves, the radar cell may contain only a few clutter scatterers, resulting in a non-Gaussian or Rayleigh distribution. Also, shadowing at low grazing angles can result in hiding large scatterers some of the time. The resulting distributions are said to have long "tails" because the probability of observing large values of the clutter amplitude is greater than with Rayleigh statistics.

A commonly used family of distributions for describing clutter power is the Weibull, which is illustrated in Figure 5-7. One form of the equation for the general Weibull distribution is [6]

$$p_\sigma(\sigma) = \begin{cases} \dfrac{b\sigma^{b-1}}{\alpha} \exp\left(-\dfrac{\sigma^b}{\alpha}\right), & \sigma \geq 0 \\ 0, & \sigma < 0 \end{cases} \tag{5.18}$$

where $\alpha = \sigma_m^b / \ln 2$, and σ_m is the median of the distribution. The parameter $a = 1/b$ is called the *width* parameter; b itself is called the *shape parameter*. The parameter $\alpha^{1/b}$ is

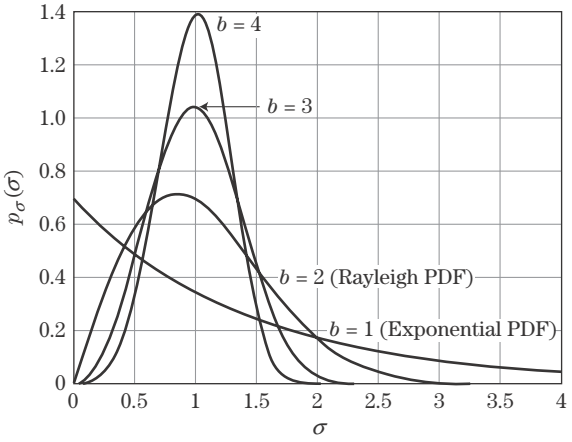

FIGURE 5-7 ■ Weibull distributions for $\sigma_m = 1$ and several values of b.

called the *scale* parameter. For a given σ_m or α, the higher the value of a and thus the lower the value of b and the longer the high value "tails" of the distribution. Figure 5-7 illustrates this for $\sigma_m = 1$. When $a = 1$ (and thus $b = 1$), the Weibull distribution reduces to the exponential PDF, while for $a = {}^1\!/_2$ ($b = 2$) it reduces to the Rayleigh PDF.

Because the Weibull is, in general, a two-parameter (b and σ_m) distribution, it can be adjusted to fit both the mean and variance of experimental data. Experimenters express the variation of clutter by choosing values of b and σ_m to best fit a Weibull distribution to their data.

Other experimenters prefer to use the log-normal distribution, another two-parameter function. The log-normal distribution is simply a distribution in which the logarithm of the return is normally distributed. It is given by [6]

$$p_\sigma(\sigma) = \frac{1}{\sigma s\sqrt{2\pi}} \exp\left(-\frac{(\ln\sigma - \bar{\sigma})^2}{2s^2}\right) \tag{5.19}$$

where $\bar{\sigma}$ is the mean RCS, and s^2 is the variance of σ.

This distribution is often used when modeling radars using a logarithmic receiver. The logarithmic receiver increases dynamic range by compressing large values of returns relative to smaller returns. An advantage of the log-normal distribution is that it models even higher "tails" than the Weibull, so it may provide a better fit to severe clutter data. Figure 5-8 gives several samples of the log-normal family, all with $\sigma_m = 1$ as in Figure 5-7.

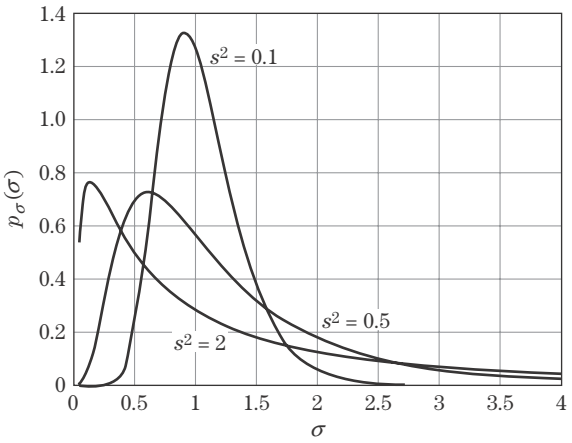

FIGURE 5-8 ■ Log-normal distributions for $\sigma_m = 1$ and several values of s^2.

When compared with Figure 5-7, it is obvious that log-normal-distributed data will exhibit a larger percentage of high values than Weibull-distributed data with the same median.

Some authors simply express the variation of clutter data in terms of the mean (or median) and the variance (or standard deviation, the square root of variance) without specifying an associated PDF. This approach is adequate for comparing the general strength and variability of different types of clutter for various conditions but does not provide enough information for analysis of radar detection performance.

5.2.2.3 Average Value Data

An extensive body of definitive experiments has been performed in the last 40 years to characterize radar clutter. Some of the key studies are as follows:

- Rain backscatter measurements from 10 to 100 GHz performed jointly by the U.S. Army Ballistic Research Laboratory (BRL) and the Georgia Tech Research Institute (GTRI) in the mid 1970s [7,8].
- Measurement of frozen precipitation by the U.S. Army Harry Diamond Laboratory millimeter waves in the late 1980s [9].
- University of Kansas measurements on terrain at high angles in the 1980s [10].
- Measurement of land clutter at low grazing angles by the Massachusetts Institute of Technology Lincoln Laboratories (MIT/LL) in the 1980s and 1990s [11].
- Naval Research Laboratory (NRL) four frequency sea clutter measurements at high grazing angles [12].
- Georgia Tech measurements of sea clutter at low grazing angles [13,14].
- The "SNOWMAN" MMW measurements performed jointly by the U.S. Army MICOM and GTRI on snow-covered ground [15].

Countless other measurement programs have been conducted in the United States and Europe. This section will attempt to summarize data from these and many other experimental programs, but the interested reader is urged to also review the references at the end of the chapter.

Land Reflectivity

Dependence on Grazing Angle Figure 5-9 shows the backscatter reflectivity of crops and short grass at X-band compiled from three data sources. The data are reported as a function

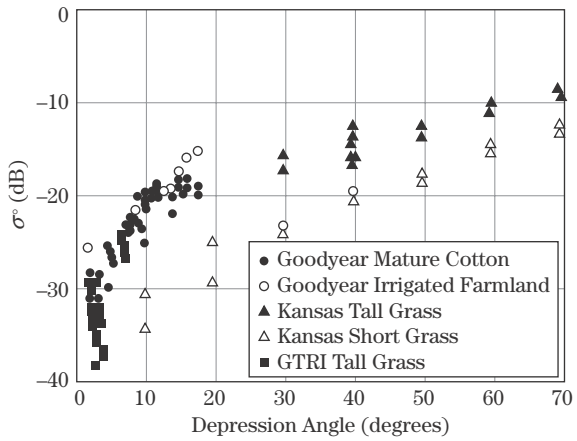

FIGURE 5-9 ■ σ^0 data for grass and crops from several sources at X-band. (Data from [16–18]. With permission.)

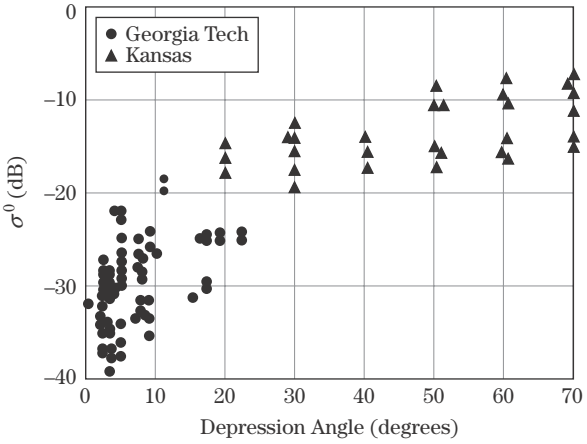

FIGURE 5-10 ■ σ^0 data for trees from two sources for X-band. (Data from [16,18]. With permission.)

of depression angle [16–18]. The data consist of time averages of individual spatial samples and exhibit the expected characteristic dependence on grazing angle shown in Figure 5-6, being relatively independent of angle above 10 degrees while rapidly decreasing in value at angles below 10 degrees. The greater spread in the data at very low depression angles is most likely due to shadowing effects.

Figure 5-10 presents backscatter reflectivity data from trees over the same angular regime as Figure 5-8. Again, the data represent time averages of spatial samples. A similar dependence is exhibited for the angular dependence as for grass and crops; however, the values for σ^0 are several dB higher, and the spatial variation is greater.

Dependence on Frequency Band Figures 5-11 through 5-14 present plots of averaged reflectivity data for five frequency bands compiled by Nathanson [15]. The data consist of σ^0 values at 0–1.5°, 3°, 10°, 30°, and 60°. Figure 5-11 gives data for relatively flat desert for L-band through X-band as a function of grazing angle. The spread in the data over the frequency range is approximately 10 dB, and the spread over 0 to 60° depression angle is more than 30 dB. Data from other sources including bare hills at L-band have yielded extremely high values for the reflectivity ($\sigma^0 > 0$ dB with corresponding RCS values of +40 dBsm) when viewing the sides of the hills at essentially 0° depression angle [16].

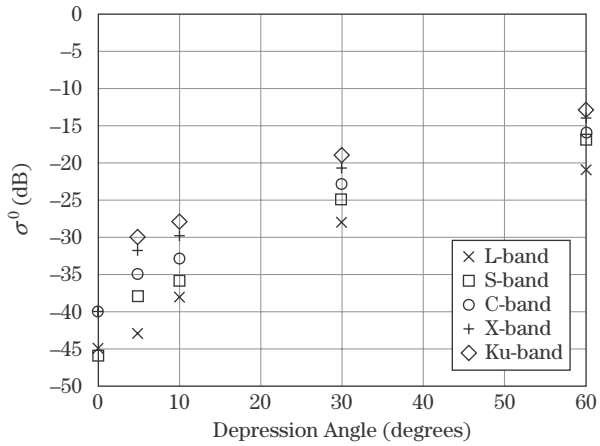

FIGURE 5-11 ■ Averaged reflectivity data for desert terrain as a function of frequency. (Adapted from Nathanson [15]. With permission.)

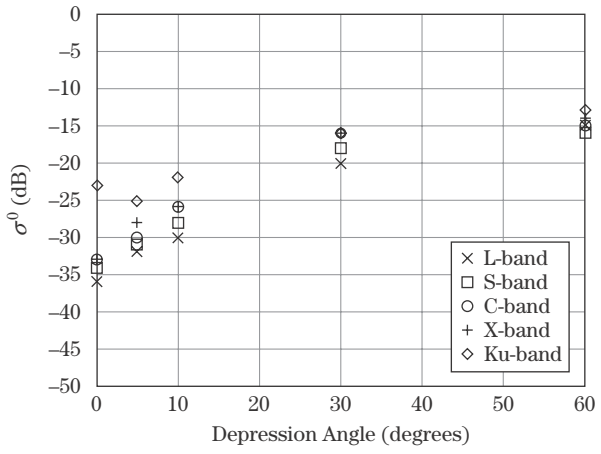

FIGURE 5-12 ■ Averaged reflectivity data for rural farmland as a function of frequency. (Adapted from Nathanson [15]. With permission.)

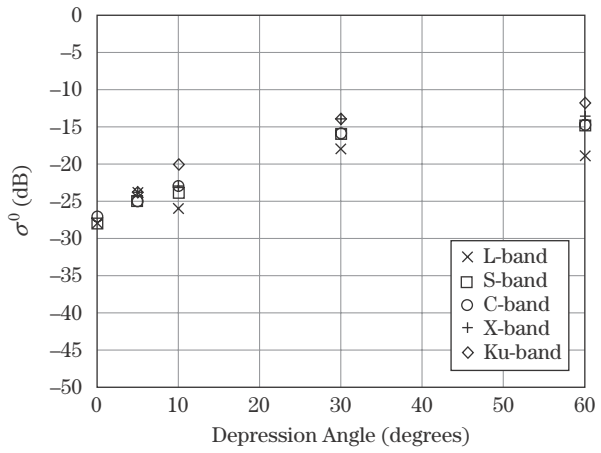

FIGURE 5-13 ■ Plot of averaged reflectivity data for heavy vegetation/jungle as a function of frequency. (Adapted from Nathanson [15]. Used with permission.)

Figure 5-12 shows averaged data for rural farmland. The spread in the data with frequency is lower than for the desert terrain, being approximately 6 dB. Also, the variation with depression angle is somewhat less, being approximately 25 dB. Figure 5-13 gives averaged data for heavy vegetation and jungle. The spread in the data with frequency is again approximately 6 dB with a similar angular variation as Figure 5-12.

Figure 5-14 gives averaged data for urban environments. The spread in the data with frequency band is lower than the previous plots, but the data are high in value as might be expected since presumably many man-made targets are included. Also, the dependence on depression angle is less than for the previous figures.

Very low angle clutter returns are of particular concern as such returns can significantly affect the detection of low flying objects such as missiles. The MIT Lincoln Laboratory performed extensive measurements in the 1980s to characterize low angle clutter over many terrain types [11]. Figure 5-15 gives σ^0 data collected by the MIT/LL for very low depression angles (0.4 to 1°) and for several frequency bands from UHF to X-band, including both vertical and horizontal polarizations. As can be seen from the figure, σ^0 appears to be at a maximum in the UHF band, decreasing at the higher frequencies, presumably due to absorption of the energy. Also, little difference is seen between

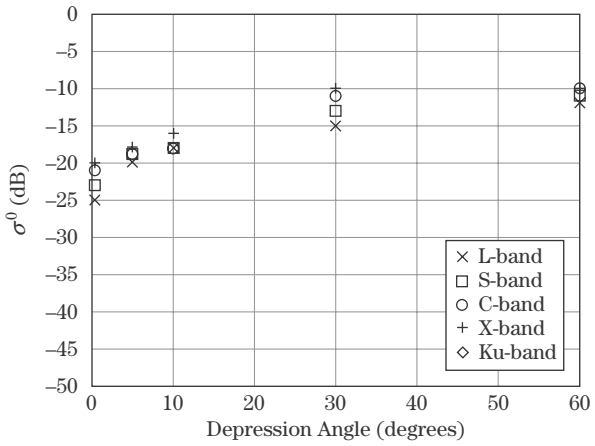

FIGURE 5-14 ■ Plot of averaged reflectivity data for urban terrains as a function of frequency. (Adapted from Nathanson [15]. With permission.)

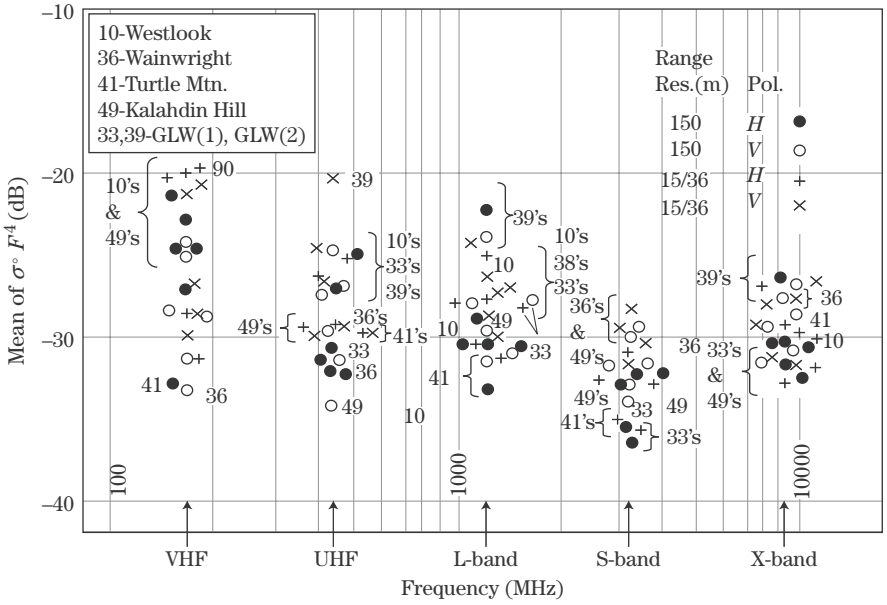

FIGURE 5-15 ■ σ^0 data for several forest/low-relief terrains at low (0.4–1°) depressions angles as a function of frequency. (From Billingsley [11]. With permission)

horizontal and vertical polarizations. Figure 5-16 gives data on mountain terrains for several frequency bands. As can be seen, the reflectivity decreases rapidly with increasing frequency, presumably caused by vegetation attenuating the returns from bare rock and ground at the higher frequencies. Note that σ^0 values of nearly 0 dB are reported at the lowest-frequency bands. Such values can often overwhelm radar MTI processors, leading to false alarms.

Sea Reflectivity The sea surface is composed of salty water with a reflection coefficient of almost −1 at microwave frequencies for small grazing angles. Thus, a smooth sea appears like an infinite flat conductive plate that scatters all of the energy impacting the surface in a forward direction so no backscatter occurs. As the wave height starts to increase, the sea begins to appear like a rough surface, and as the wave height continues to grow, organized

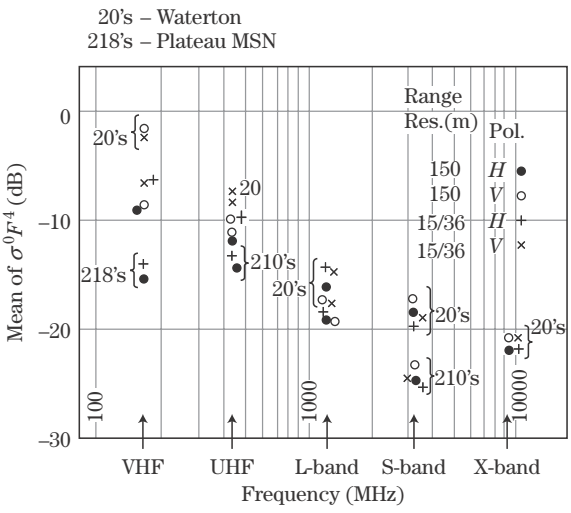

FIGURE 5-16 ■ σ^0 data for two mountain terrains at low (1.2°) depressions angles as a function of frequency. (From Billingsley [11]. With permission.)

TABLE 5-2 ■ Parameters Affecting Sea Return

PARAMETER	COMMENTS
Wave height	Strong proportional dependence
Wind speed	Dependence increases with increasing frequency
Wind/wave look direction	Significant difference between up-wave and down-wave
Polarization	Dependence decreases with increasing frequency
Grazing angle	Strong dependence at low angles, weaker dependence in the plateau region
Frequency band	Proportional to frequency in the microwave region

wavefronts occur that provide a strong directional dependence to the scattering. Table 5-2 gives the primary physical parameters that can affect sea return.

As can be seen from Table 5-2, wave height is one of the major physical parameters affecting sea return. Unfortunately, wave height is often difficult to measure during experiments. In addition, wave height is irregular. The wave height is considered to be the "significant wave height," which is an estimate of the average peak-to-trough height of the largest one-third of the observed waves.

Since it is easier to estimate a range of wave heights than a specific wave height, sea return data are often give in terms of *sea state*. The Douglas sea number [6] is a specific, widely used scale of sea states, correlated wind speeds, and subjective descriptions in which each defined sea state represents a range of wave heights as given in Table 5-3.[2] Note that sea states are defined only for a fully developed sea, that is, a sea over which a constant wind has been blowing long enough to build waves to their maximum height and the distance over which the wind has been blowing (called the *fetch*) is far enough to build waves to their maximum value.

[2]Other sea scales exist, such as the Beaufort scale and the World Meteorological Organization (WMO) scale. The WMO scale generally adopts the Douglas sea-scale definitions.

TABLE 5-3 ■ Douglas Sea State versus Wave Height and Wind Speed for a Fully Developed Sea

Sea State	Significant Wave Height (ft)	Wind Speed (Kts)
0	0 to 0.5	0 to 2
1	0.5 to 1	2 to 7
2	1 to 3	7 to 12
3	3 to 5	12 to 16
4	5 to 8	16 to 20
5	8 to 12	20 to 25
6	12 to 20	25 to 32
7	20 to 40	32 to 45
8	40+	45+

Source: Adapted from Long [6] (with permission).

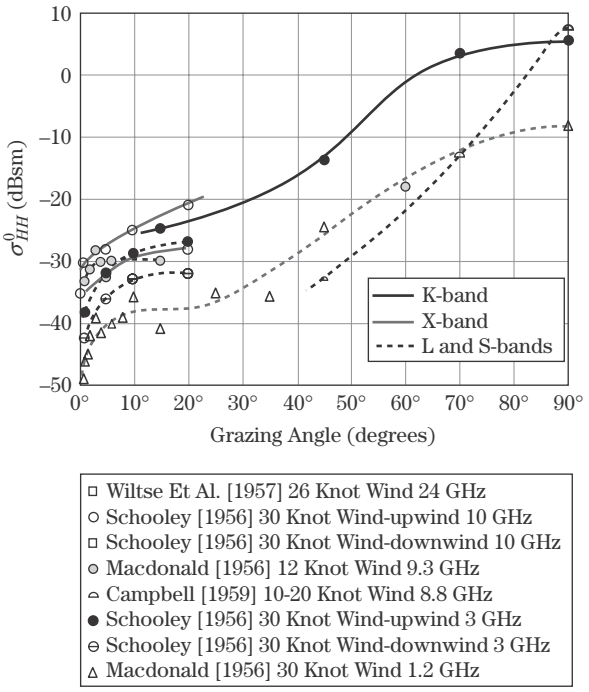

FIGURE 5-17 ■ Sea return as a function of grazing angle for four radar bands. (From Long [6]. With permission.)

Angular and Frequency Dependencies Figure 5-17 gives horizontally polarized sea return data from several original sources for four radar bands as a function of grazing angle, wind speeds corresponding to high sea states, and upwind versus downwind directions. The data illustrate strong angular, frequency, and look direction dependence. Note that very high values of σ^0 (above 0 dB) are seen at nadir. This suggests that sea clutter could be a significant limitation when searching for a small, slow-moving target on the sea surface. In addition to high backscatter, shadowing and sea Doppler accentuate the detection problem.

Figure 5-18 presents a plot of averaged data for sea clutter from Nathanson [15] for five radar bands as a function of depression angle for sea state 1. For this low sea state, σ^0 is relatively small, particularly for low depression angles. Note that there is much more

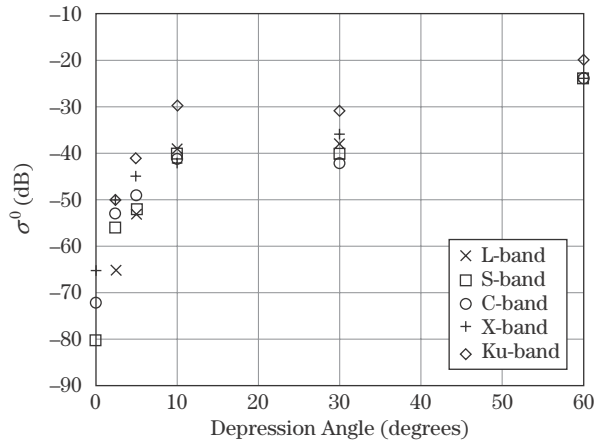

FIGURE 5-18 ■ Averaged sea return as a function of depression angle and radar band, sea state 1, VV polarization. (Adapted from Nathanson [15]. With permission.)

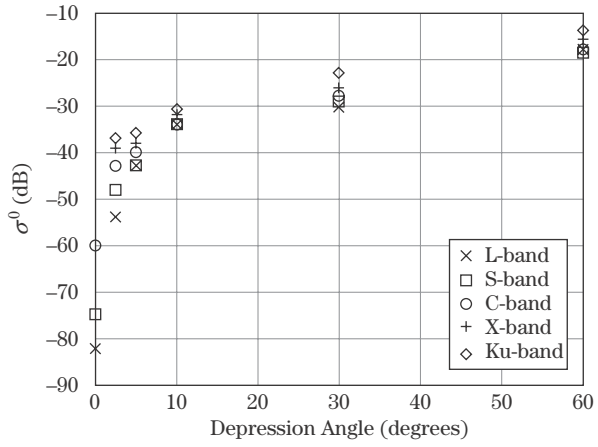

FIGURE 5-19 ■ Averaged sea return as a function of depression angle and radar band, sea state 3, VV polarization. (Adapted from Nathanson [15]. With permission.)

variation with frequency at the lower depression angles. Figure 5-19 gives averaged sea return data for sea state 3. These data are almost 10 dB higher than for sea state 1. The frequency dependencies appear to be similar to those for Figure 5-18.

Figure 5-20 compares values of σ^0 for vertical and horizontal polarized returns from sea clutter at L- and X-bands. As was discussed previously, there is a much greater difference between the vertical and horizontal values of σ^0 at L-band than there is at X-band.

One important parameter for sea return is the range fall-off of sea clutter echo power. As range increases, the grazing angle δ at which the sea surface is viewed decreases. When δ falls below the critical angle, θ_C, the surface becomes "smooth" by the Rayleigh criterion of equation (5.15). Figure 5-21 gives the measured sea data as a function of range dependence for two regions: above and below the critical angle; and low and high wave heights [19]. Note that the range for the critical angle moves in (higher depression angle), and the wave height (and thus, the rms surface roughness) increases as predicted by equation (5.16). These data show that, below the critical angle, the R^{-3} range dependence of pulse-limited sea clutter return transitions to approximately an R^{-7} dependence so that the clutter return rapidly becomes insignificant. In addition, the critical angle often appears near the first multipath null angle, further enhancing the clutter roll-off with range. (See Chapter 4 for a discussion of multipath.)

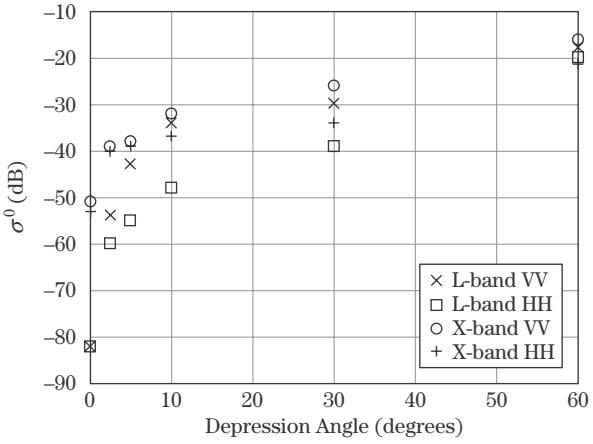

FIGURE 5-20 ■ Sea return as a function of depression angle for VV and HH polarizations, land X-bands, sea state 3. (Adapted from Nathanson [15]. With permission.)

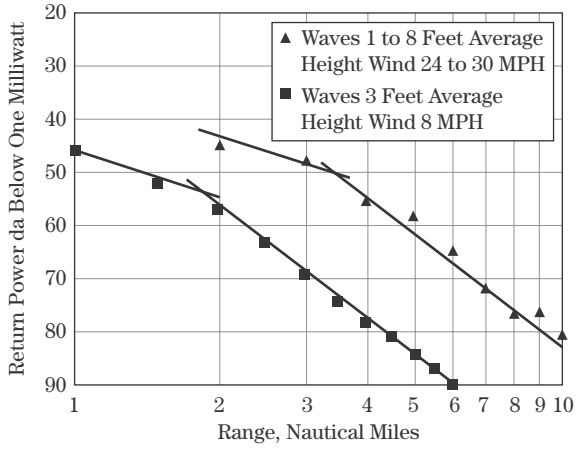

FIGURE 5-21 ■ Range dependence of sea return for two wave conditions, X-band, HH polarization. (From Dyer and Currie [19]. With permission.)

Ducting Because the sea surface has a strong reflection coefficient and water vapor is always present near the surface, conditions can occur such that a high water concentration and thus a reflective layer occur over some region above the water. When this happens, the high water concentration layer and the sea surface act like a two-dimensional waveguide, trapping the radiofrequency (RF) energy and extending the range of sea return detection. The reflection coefficient of the sea determines the duct shape and transmission efficiency. Figure 5-22 shows two sets of sea return data as a function of grazing angle taken with the same radar, the only difference being the lapse of several hours in time. The morning data show much less dependence on angle than the afternoon data. Apparently, ducting conditions were present in the morning but were absent in the afternoon. These data were collected in February in Wildwood, New Jersey, showing that ducting can occur in cold as well as tropical conditions.

Figure 5-23 gives a summary of range dependence measurements above and below the critical angle performed in Boca Raton, Florida, over a period of several years at X-band. Range dependencies quite different from the expected R^{-3} for a pulse-limited radar occurred a significant portion of the time, indicating both ducting conditions and possibly variations in the multipath field from time to time.

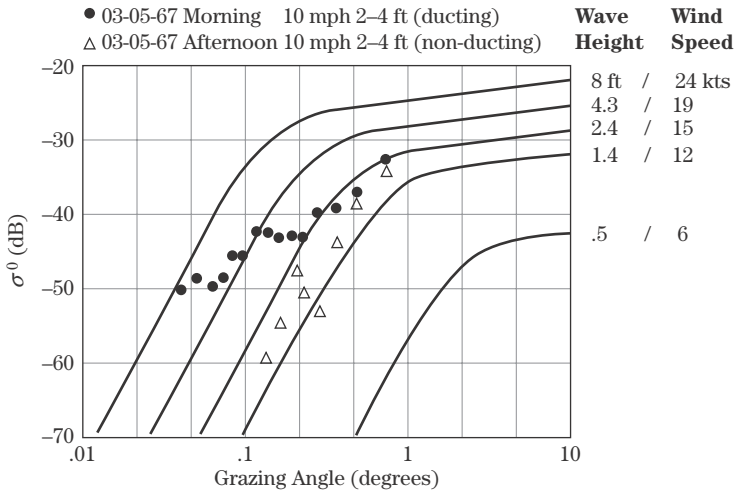

FIGURE 5-22 ■ Comparison of sea return achieved under ducting and nonducting conditions, X-band, HH polarization. (From Dyer and Currie [19]. With permission.)

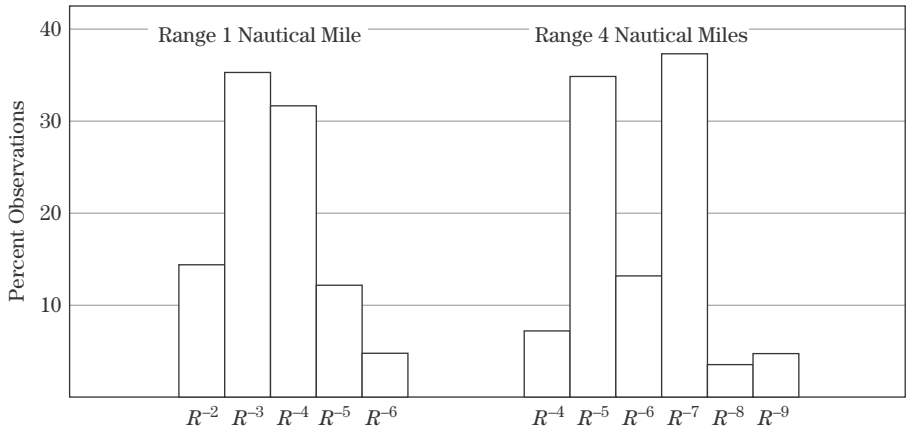

FIGURE 5-23 ■ Measured range dependencies above and below the critical grazing angle as a percentage of total measurements. (From Dyer and Currie [19]. With permission.)

5.2.2.4 Clutter Variability Properties

In the previous section average values for surface clutter were discussed, but the variability of clutter reflectivity with time and or space is as least as important, if not more so. These topics are addressed in this section.

Land Clutter Variations

Temporal Variations Land clutter generally contains some vegetation. Consequently, land clutter returns will vary with time due to wind-blown motion of leaves, needles, branches, and stalks. Since such motion makes detection more difficult, it must be described and allowances made for it when calculating the probability of detection for a target in clutter. The probability density function, $p_\sigma(\sigma)$, and the cumulative distribution function (CDF), $P_\sigma(\sigma)$, are used to describe the variation in RCS or power. Figure 5-24 illustrates an estimated unnormalized probability density function obtained as the histogram of the measured data, which is just a plot of the number of independent clutter samples that fall within a series of narrow power intervals. If the histogram is normalized by dividing the sample counts by the total number of samples times the width of an amplitude bin, an estimate of the PDF is obtained.

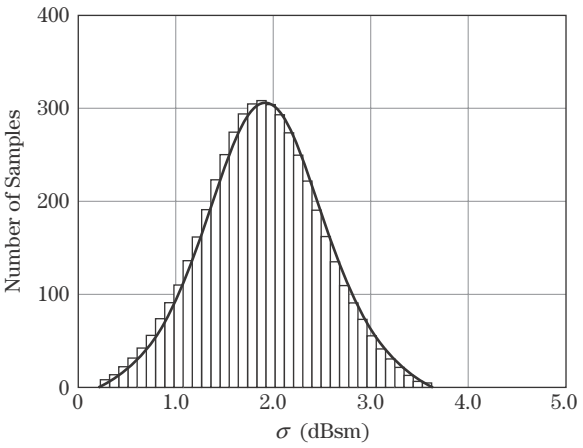

FIGURE 5-24 ■ A histogram provides an estimate of an unnormalized probability density function.

The CDF is the integral of the PDF,

$$P_\sigma(\sigma) = \int_{-\infty}^{\sigma} p_\sigma(v)\, dv \tag{5.20}$$

Values of the CDF increase monotonically from zero to one. If the area under the normalized histogram from the lowest value to some value σ is calculated, an estimate of the CDF is obtained. Cumulative distributions are quite useful because some key parameters are easily read from a plot of the CDF. For instance, the median value is the 50% point ($P_\sigma(\sigma) = 0.5$) on the curve. Rivers [20] observed that for log-normal and Weibull distributions with parameters appropriate for modeling measured sea clutter, the mean value of the power, $\bar{\sigma}$, can be estimated from the value corresponding to the 90% point on the CDF, $\sigma_{0.9}$, to be 3.5 dB below the 90% point by the relation

$$\bar{\sigma} = (\sigma_{0.9} - 3.5 \text{ dB}) \pm 0.5 \text{ dB} \tag{5.21}$$

Newer land clutter data observed by Billingsley [11] is spikier than that used by Rivers, suggesting that the ±0.5 dB tolerance in equation (5.21) should be wider [6]. As another example of the usefulness of CDFs, the standard deviation in dB of a log-normal distribution is $\sigma_{0.84} - \sigma_{0.16}$.

Figure 5-25 gives a measured CDF for wind-blown trees at X-band. The dotted line approximates the CDF corresponding to an exponential PDF in this plot format. The data in Figure 5-25 appear approximately exponential in their general shape, but their distribution is seen to be wider than exponential. For example, the 90% mark on the CDF occurs at about –39 dB for the exponential distribution, but not until the larger value of –30 dB for the X-band tree data. Variable clutter complicates detection in two ways. First, since the return is changing with time, part of the time the reflectivity will be larger than the average value. Second, the rate of fluctuation can limit the effectiveness of Doppler processing.

Table 5-4 gives the standard deviations (square root of the variance) measured for wind-blown vegetation as a function of frequency and polarization. The standard deviation for an exponential distribution, converted to a decibel scale, is approximately 5.7 dB [6]. Thus, at 9 GHz the distributions appear narrower than exponential, but at 95 GHz and higher they are wider than exponential.

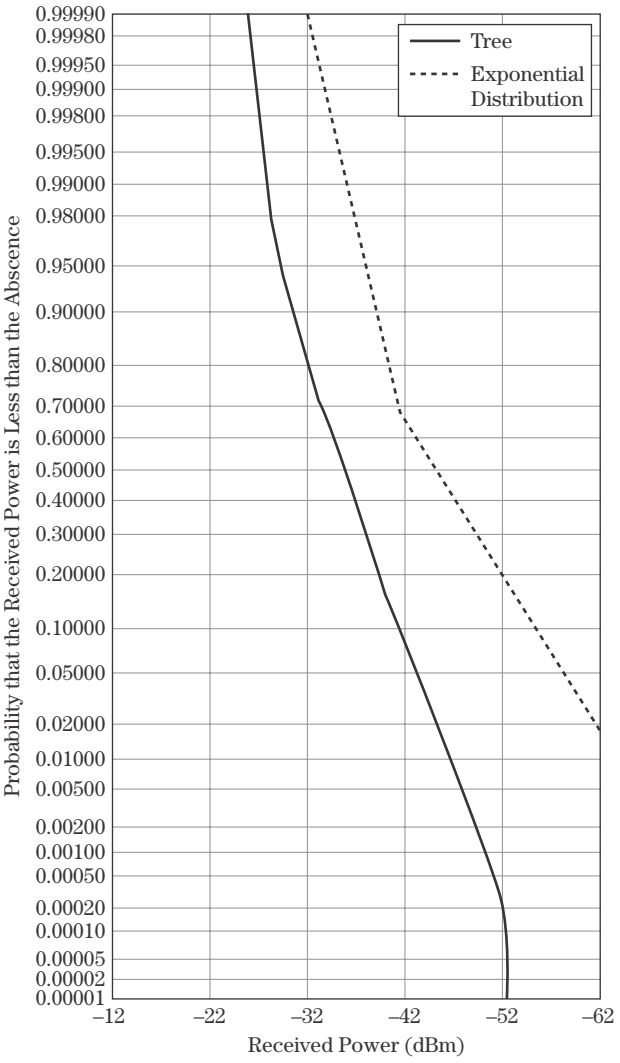

FIGURE 5-25 ■ Cumulative probability distribution for deciduous trees at X-band, 4.1° depression angle. (From Currie et al. [21]. With permission.)

Decorrelation Time An important metric of clutter temporal properties is the decorrelation time. The decorrelation time, τ_0, is defined as the time lag required for the autocorrelation function of a set of clutter samples to decay to some defined fraction, usually 0.5 or $1/e = 0.367$ of its peak value at zero lag. The autocorrelation function $\phi_{cc}(\tau)$ of the time-varying clutter return, $c(t)$, measures how similar successive data samples are to a first sample as the delay time between samples increases. The power spectral density function is the Fourier transform of $\phi_{cc}(\tau)$,

$$S_{cc}(f) = \int_{-\infty}^{+\infty} \phi_{cc}(\tau)\, e^{-j2\pi f \tau} d\tau \tag{5.22}$$

where τ is the autocorrelation lag time.

If the clutter power spectrum is "white" (constant) over the receiver bandwidth B, then the decorrelation time equals $1/B$. This is the same as the case for random noise.

TABLE 5-4 ■ Measured Standard Deviations of Temporal Variations for Trees

		Average Value of Standard Deviation (dB)			
Frequency Clutter Type	Polarization	9.5 GHz	16.5 GHz	35 GHz	95 GHz
Deciduous trees, summer	Vertical	3.9	—	4.7	—
	Horizontal	4.0	—	4.0	5.4
	Average	4.0	—	4.3	5.4
Deciduous trees, fall	Vertical	3.9	4.2	4.4	6.4
	Horizontal	3.9	4.3	4.3	5.3
	Average	3.9	4.2	4.3	5.0
Pine trees	Vertical	3.5	3.7	3.7	6.8
	Horizontal	3.3	3.8	4.2	6.3
	Average	3.4	3.7	3.9	6.5
Mixed trees, summer	Vertical	3.3	—	4.0	—
	Horizontal	4.6	—	4.2	—
	Average	4.4	—	4.1	—
Mixed trees, fall	Vertical	4.1	4.1	4.7	6.3
	Horizontal	4.5	4.3	4.6	5.0
	Average	4.4	4.2	4.6	5.4
Field, tall grass	Vertical	1.5	—	1.7	2.0
	Horizontal	1.0	1.2	1.3	—
	Average	1.3	1.2	1.4	2.0
Rocky area	Vertical	1.1	2.2	1.8	1.6
	Horizontal	1.2	1.7	1.7	1.7
	Average	1.1	1.9	1.8	1.7
10-in. corner reflector located in grassy field		1.0	1.0	1.2	1.2

Source: From Currie et al. [21] (with permission).

Because the receiver bandwidth also determines the Nyquist rate of its output, the received signal output will normally be sampled at a rate of about $1/B$ samples per second (see Chapter 14). Since the samples are spaced by the decorrelation time, the sampled data will appear uncorrelated with a white power spectrum. If the clutter instead has a decorrelation time greater than $1/B$ seconds, then the sampled clutter data will not appear white and will have some degree of correlation from one sample to the next.

The decorrelation time is important for detection analysis because it determines the number of uncorrelated samples, N_i, available for integration for signal-to-clutter improvement according to

$$N_i = \begin{cases} \dfrac{N_t PRI}{\tau_0}, & PRI \le \tau_0 \\ N_t, & PRI \ge \tau_0 \end{cases} \tag{5.23}$$

where N_t is the total number of clutter samples and PRI is the time between samples. As will be seen in Chapter 15, coherent or noncoherent integration of radar data can improve the detectability of targets in the presence of interference, provided that the interference samples are uncorrelated so they can be made to "average out" while the target signal is reinforced. Thus, if the total sample collection time $N_t PRI$ is shorter than the decorrelation time, no uncorrelated clutter samples are obtained, and no improvement in target detectability is gained by integration of successive samples.

If the clutter does decorrelate during the collection time, then some improvement in target detectability is possible by integrating multiple samples. In coherent integration, the complex (in-phase [I] and quadrature [Q]) data are integrated (added) to cause the target component of the samples to add in phase, whereas the uncorrelated clutter and noise components do not add in phase. In this case, the signal-to-clutter ratio (SCR) and signal-to-noise ratio (SNR) (and thus signal-to-interference ratio [SIR]) are increased, significantly improving target detectability. In noncoherent integration, the magnitude or magnitude squared of the complex receiver output data is taken and then integrated. Discarding the phase information eliminates the possibility of a gain in SCR. Nonetheless, an improvement in target detectability is still achieved, though less than in the coherent integration case. Chapter 15 discusses the effects of coherent and noncoherent integration on target detection in white interference in greater detail.

Figure 5-26 presents the autocorrelation functions for windblown trees in conditions described as a "windy day," while Table 5-5 gives the 50% ($\tau_{1/2}$) and $1/e$ ($\tau_{1/e}$) decorrelation times in seconds. As can be seen, essentially no integration improvement could be achieved at the lower frequency bands, and only limited improvement could be achieved at X-band.

Figure 5-27 gives measured decorrelation times for higher frequencies (10 GHz through 95 GHz) as a function of wind speed. As can be seen, at the higher frequencies much shorter decorrelation times are observed, an advantage for obtaining better noncoherent integration efficiency.

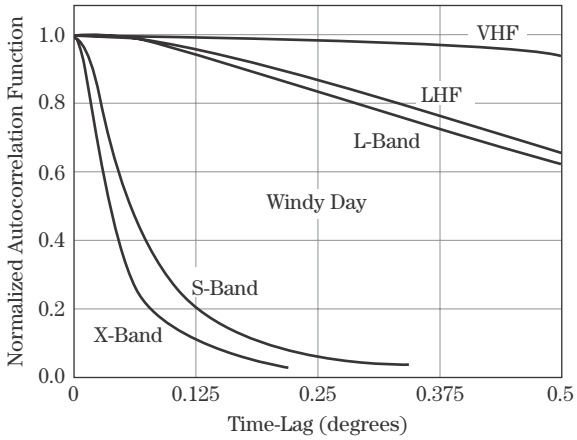

FIGURE 5-26 ■ Autocorrelation functions of the returns from windblown trees for several frequency bands on a windy day. (From Billingsley [11]. With permission.)

TABLE 5-5 ■ Measured Decorrelation Times at Five Frequency Bands

Frequency Band	Correlation Time(s)	
	$\tau_{1/2}$	$\tau_{1/e}$
VHF	4.01*	5.04*
UHF	0.69	0.94
L-Band	0.67	0.95
S-Band	0.062	0.081
X-Band	0.033	0.049

Note: * = extrapolated estimate
Source: From Billingsley [11] (with permission).

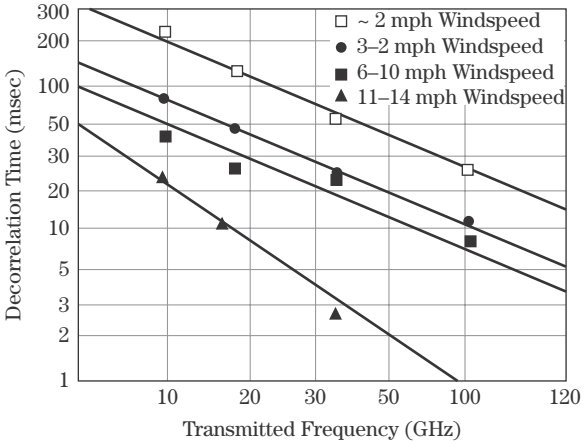

FIGURE 5-27 ■ Decorrelation time for windblown trees as a function of wind speed. (From Currie et al. [21]. With permission.)

Clutter Frequency Spectra A second way to look at temporal variations in clutter returns is in terms of clutter power spectra. Power spectra tell us how rapidly a return is varying. This is of interest since many radars use Doppler processing to improve target detection in heavy clutter. Clutter spectra are of interest for two situations: (1) very slow-moving targets such as ground vehicles or boats; and 2) high-speed targets that may be affected by aliasing ("foldover") of the clutter spectra around the pulse repetition frequency (PRF). (See Chapter 8 for a discussion of Doppler foldover.)

Theoretical formulations of clutter spectra yield Gaussian-shaped spectra, yet a number of actual clutter measurements have yielded power law-shaped spectra. These differences are of concern since power law spectral shapes roll off more gradually with frequency than Gaussian spectra. This problem was first identified by Fishbein et al. [22] when attempting to develop models for the spectral data on trees at X-band shown in Figure 5-28 [22]. They found that a Gaussian curve fit rolled off much too rapidly. A much better fit was obtained with a power law curve of the form

$$S_{cc}(f) = \sigma_{DC}\left(\frac{1}{1+\left(\frac{f}{f_c}\right)^n}\right) \tag{5.24}$$

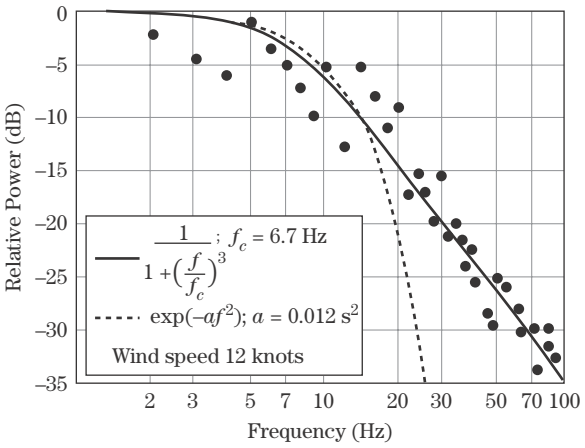

FIGURE 5-28 ■ Spectral data from trees at X-band with Gaussian and power function curve fits. (From Fishbein et al. [22]. With permission.)

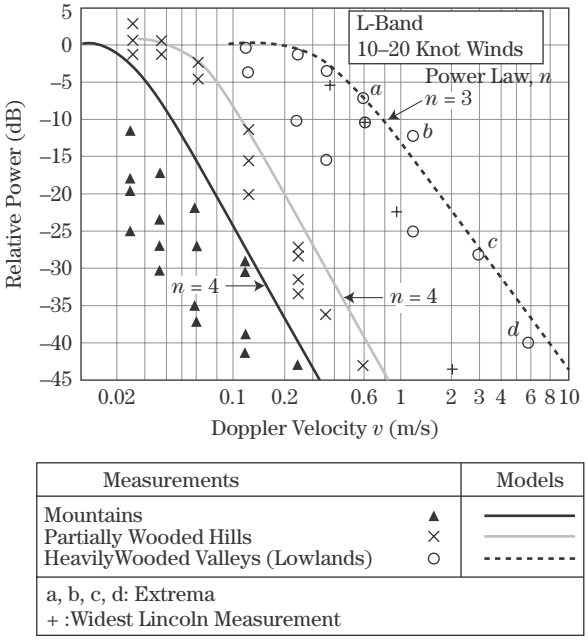

FIGURE 5-29 ■ L-band spectral data with various power law curve fits. (From Simpkins et al. [23]. With permission.)

where σ_{DC} is the DC clutter power return, f_c is the 3 dB cutoff frequency for the power spectrum, and n is an integer selected to best fit the data. Fishbein et al. found that a value of $n = 3$ fit the data best. Other experimenters have also measured power law dependencies. Figure 5-29 presents power spectral data at L-band for woods and wooded hills measured by the U.S. Air Force's Rome Air Development Center (RADC) [23]. For these data, the best power law fits were obtained with $n = 3$ or 4.

Table 5-6 presents the cutoff and power law exponents determined for wind-blown tree data at 10 GHz though 95 GHz for both logarithmic and linear receiver transfer functions. The exponent seems to lessen with increasing frequency, implying a slower roll-off, while the logarithmic receiver provides a steeper roll-off than the linear case.

To date, theorists have not been able to determine a theoretical basis for power law frequency dependence, yet experimenters continue to observe them in measured data. One possibility is that Doppler spectra can be significantly affected by radar system imperfections such as nonlinearities, dynamic range limits, and oscillator phase noise. Recently, Billingsley [11] measured tree data with a high-quality coherent instrumentation radar having high linearity over a wide dynamic range, stabilized oscillators, and low-sidelobe narrow Doppler filters. He obtained clutter power spectra that were well modeled by a

TABLE 5-6 ■ Corner Frequencies and Power Exponents for Tree Return Spectra

Power Function Parameter	Frequency			
	9.5 GHz	16 GHz	35 GHz	95 GHz
n (linear)	3	3	2.5	2
n (log)	4	3	3	3
f_c (Hz), 6–15 mph wind speed	9	16	21	35

Source: From Currie et al. [21] (with permission).

two-sided exponential roll-off. This spectrum has a rate of decay that falls between the Gaussian and power law models.

These observations suggest that equipment imperfections may be a significant contributor to the slower decay of data that are well modeled by power law spectra. However, many fielded systems will suffer these limitations, so a practical approach to performance assessments could use both Gaussian and power law clutter power spectrum models to establish upper and lower bounds on performance in the presence of clutter.

Spatial Variations As discussed earlier, when the radar scans across the surface, the number and types of scatterers within the radar beam change, resulting in a changing return. These variations are described using the same tools as for temporal variations (i.e., amplitude distributions and spatial correlation functions).

Spatial amplitude distributions can be much wider than temporal distributions, particularly at lower grazing angles where shadowing and multipath come into play. Most experimenters resort to Weibull distributions to describe the variations. A key finding of experimenters is that at higher grazing angles, spatial distributions tend to appear exponential (Weibull width parameter $a \approx 1$) while at low grazing angles the width parameter increases greatly. The calculated spatial distributions by Booth [24] for cultivated land at X-band in Figure 5-30 illustrate this effect. They are approximately exponential-distributed (width parameter $a \approx 1$) at a grazing angle of 5° but become much wider at lower angles.

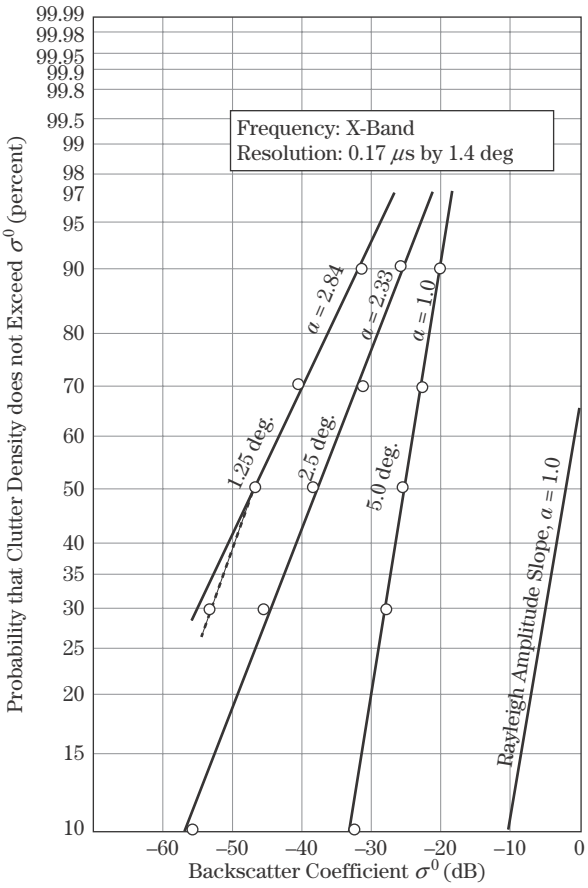

FIGURE 5-30 ■ Spatial distributions of cultivated land as function of grazing angle X-band. (From Booth [24]. With permission.)

TABLE 5-7 ■ Spatial Statistical Attributes for X-Band Ground Clutter

Terrain Type	Depression Angle (deg)	Weibull Parameters			Ensemble Mean Clutter Strength	Percent of Samples above Radar Noise Floor	Number of Patches
		a	σ_m (dB)	σ_w^0 (dB)	σ^0 (dB)		
Rural/	0.00–0.25	4.8	−60	−33	−32.0	36	413
Low-Relief	0.25–0.50	4.1	−53	−32	−30.7	46	448
	0.50–0.75	3.7	−50	−32	−29.9	55	223
	0.75–1.00	3.4	−46	−31	−28.5	62	128
	1.00–1.25	3.2	−44	−30	−28.5	66	92
	1.25–1.50	2.8	−40	−29	−27.0	69	48
	1.50–4.00	2.2	−34	−27	−25.6	75	75
Rural/	0–1	2.7	−39	−28	−26.7	58	176
High-Relief	1–2	2.4	−35	−26	−25.9	61	107
	2–3	2.2	−32	−25	−24.1	70	44
	3–4	1.9	−29	−23	−23.3	66	31
	4–5	1.7	−26	−21	−22.2	74	16
	5–6	1.4	−25	−21	−21.5	78	9
	6–8	1.3	−22	−19	−19.1	86	8
Urban	0.00–0.25	5.6	−54	−20	−18.7	57	25
	0.25–0.70	4.3	−42	−19	−17.0	69	31
	0.70–4.00	3.3	−37	−22	−24.0	73	53

σ_m = median reflectivity
σ_w^0 = mean reflectivity
F = propagation factor (see Chapter 4)
Source: Adapted from Billingsley [11] (with permission).

The effect of grazing angle on the PDF is further illustrated by Table 5-7, which gives spatial statistics for rural and urban settings as a function of grazing angle for very low angles. For rural settings, and angles above 5 degrees, the Weibull width parameter a indicates an approximately exponential power PDF ($a \approx 1$), while the PDF becomes much wider for lower angles. As might be expected, the urban setting exhibits larger width parameters and thus distributions wider than exponential even at 4°. Thus, in general, exponential power statistics are expected in the plateau regions for all but urban clutter, but much wider distributions are seen for low grazing angles. For urban settings, wide distributions may be observed even in the plateau region because of the height of man-made structures that cause shadowing even at higher grazing angles.

Sea Clutter Variation The return from the sea varies in time due to the effects of the wind on sea waves. These effects are of several types: waves created by the wind blowing for a period of time over a given "fetch" of water, ripples that appear on the surface due directly to the wind, white caps created when the tops of waves break over the front of the waves, and airborne spray that results from ripples and white caps.

Initially, amplitude (voltage) statistics from a fixed range-azimuth cell were assumed to be Rayleigh. This model fit measured data for low-resolution radars well. However, as finer-resolution radars came into use over time, non-Rayleigh statistics were encountered. The current view is that wind-produced ripples on the sea surface produce noise-like variations in sea return or "speckle" that are approximately Rayleigh distributed in amplitude but that the large-scale moving structure of the sea swells changes the local slope of the

rippled surface, imposing a time-varying change in the mean of the Rayeigh PDF in a give spatial cell. The resulting amplitude statistics of the return are non-Rayleigh, implying a non-Gaussian model of the complex I/Q data.

In general, the amplitude statistics are observed to become "spikier" with decreasing grazing angle and decreasing radar footprint area, possibly due to a decreasing average or median clutter value while the strength of the sea clutter spikes remains relatively constant. Also, horizontal polarization tends to present spikier clutter than does vertical polarization, particularly at low grazing angles. Sea clutter statistics also vary with the radar-wind/wave look direction.

Experimenters have used Weibull, log-normal, and K distributions to model sea statistics. In particular, Ward et al. [25] and Ward [26] performed extensive modeling of sea return using the K distribution, a two-parameter distribution that can be related to the Weibull and the log-normal. It is given by [6]

$$p_\xi(\xi) = \begin{cases} \dfrac{2b}{\Gamma(v)} \left(\dfrac{b\xi}{2}\right)^v K_{v-1}(b\xi), & \xi > 0 \\ 0, & \xi < 0 \end{cases} \tag{5.25}$$

where

$\xi = \sqrt{\sigma}$ is the clutter amplitude.
v is the "shape factor."
b is a scale factor.
$\Gamma(\cdot)$ is the gamma function.
K_n is the modified Bessel function of the third kind and order n.

Ward showed that this distribution describes the statistics of the product of two random variables, one described by a Rayleigh PDF and the other by a chi or gamma PDF [26]. Thus, the Rayleigh component can be used to model the speckle portion of the sea return, while the chi component can be used to model the time-varying mean of the local Rayleigh PDF due to large-scale sea structure, as discussed previously. The K distribution is believed to provide a better fit to sea clutter data, particularly for high resolution radars. See [25–27] for more information.

Temporal Variations

Correlation Properties Work on calculating autocorrelation functions for sea returns has demonstrated that there are three mechanisms involved: (1) return from sea spray and white caps; (2) specular returns (spikes) from wavefronts; and (3) Bragg scattering [28]. The return from sea spray and Bragg scattering decorrelates very rapidly, while the specular return from the wavefront is highly correlated in time. Figure 5-31 illustrates this effect. The figure shows the autocorrelation function for sea return at K_u-band on two time scales. The upper scale indicates that almost 600 ms are required for the return to decorrelate to 50% of the ACF peak. The lower scale shows that the return drops from a normalized correlation of 1 to 0.85 in approximately one ms. The initial 15% decorrelation is due to the rapidly moving sea spray, while the longer 50% decorrelation time is due to the much slower motion of the wavefronts. Attempts have been made to use frequency agility to decorrelate sea return, but only the decorrelation due to sea spray and speckle is affected. Thus, sea waves tend to be highly correlated over many milliseconds, so that only scan-to-scan integration will be effective in increasing target detectability.

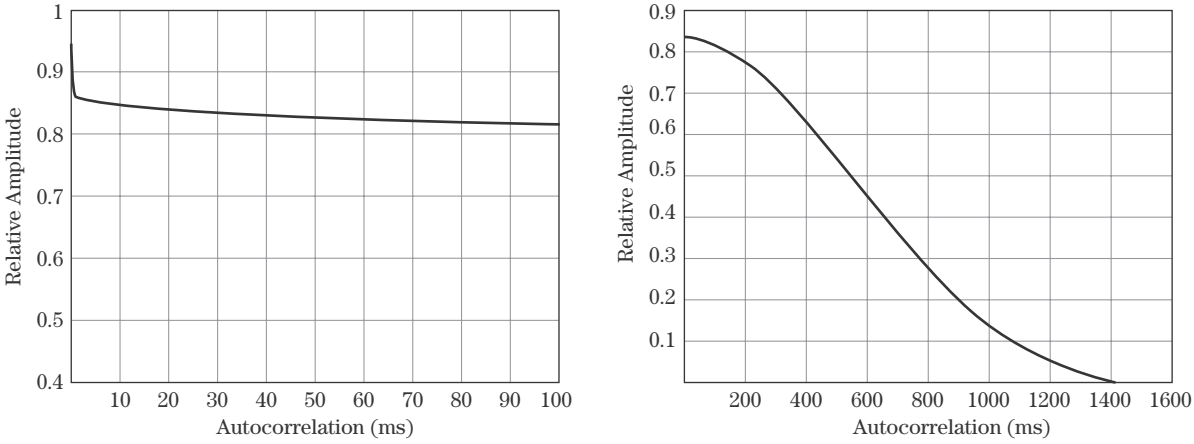

FIGURE 5-31 ■ Autocorrelation function of sea return at K_u-band. 3.9° depression angle, and downwind/down-wave look direction. (From Ward et al. [25]. With permission.)

Spectral Properties The spectrum for sea clutter differs from that of land since sea waves can move physically toward or away from the radar. Thus, sea clutter can have a nonzero average Doppler frequency, unlike land clutter where moving scatterers are anchored in place. The Doppler frequency at which the motion of scatterers at a radial velocity, v, appears is given by the equation

$$f_d = \frac{2v}{\lambda} \tag{5.26}$$

Consequently, the width, Δf_d, of the Doppler spectrum is related to the width, Δv, of the velocity spectrum according to

$$\Delta v = \frac{\lambda}{2}\Delta f_d \tag{5.27}$$

Figure 5-32 gives an example of the coherent spectrum at L-band, indicating the spectrum width for various amplitude levels [29]. At higher frequencies the center frequency and spectral width would be expected to scale proportional to the transmitted frequency in accordance with equations (5.26) and (5.27). While the spectra in this figure are approximately symmetric and Gaussian in shape, sea clutter spectra, especially at fine resolution and low grazing angle, are often distinctly asymmetric; see [28] for a number of examples.

Sea Spikes *Sea spikes* are strong returns from highly localized points or regions on the sea surface. The region generating the spike is usually, but not always, much smaller than the resolution cell area. Spikes are a problem for radar detection because they can exceed the signal level of small targets and can last for many seconds. Explanations of the causes for such returns are disputed by various researchers and have included returns from white caps, to sea spray, to returns from particular facets located on the wavefronts. Most likely all are responsible. Some general properties of sea spikes from the radar point of view reported by Werle [30] are as follows:

- Spikes occur significantly more often for horizontal than for vertical polarization.
- Spike intensity is usually greater for horizontal than for vertical polarization.
- HH/VV polarization ratios of greater than 10 dB were observed.

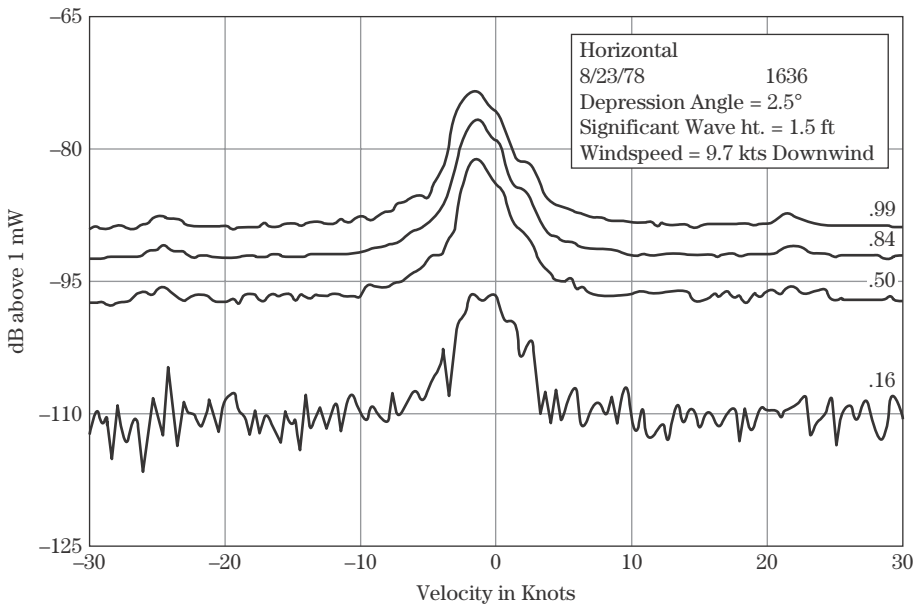

FIGURE 5-32 ■ Percentile of Doppler spectra at L-band. (From Plummer et al. [29]. With permission.)

- Spikes at both HH and VV occurred much less often than for HH alone.
- Rarely was a VV spike seen without a concurrent HH spike.

Walker [28] sates that the HH/VV intensity difference holds for the specular and Bragg scattering components but that the white cap component has roughly equal HH and VV backscatter. Given these properties, use of a dual-polarized radar and analysis of measured HH/VV polarization ratios may be one technique for recognizing and removing spikes from clutter data.

Spatial Variations Sea clutter returns are due to moving scatterers: the wind-driven spray and the gross and fine shape of the moving waves. Consequently the temporal and spatial variations of sea clutter are correlated. The only major difference between the two is due to wind-wave look direction. Generally, upwind/up-wave provides the highest radar return while downwind/down-wave provides the lowest return. This occurs because waves lean away from the wind so that the more vertical wavefronts are exposed in the upwind/up-wave direction, while the sloping backs are exposed in the downwind/down-wave direction.

5.2.3 Atmospheric Clutter

Atmospheric clutter primarily consists of hydrometeors, of which rain is the primary case of interest. Other atmospheric phenomena such as *angels* (clear air returns of unknown origin) can be of concern but will not be covered here. Frozen precipitation is also of interest, but primarily at millimeter wave frequencies because of the lower reflectivity of ice compared with water in the microwave bands. Experiments to determine average reflectivity as well as the spectral properties of rain are discussed in the following sections.

5.2.3.1 Average Value Data

Rain Reflectivity Average Values Raindrops can be modeled as dielectric spheres of differing sizes that are contained within the radar resolution cell. The radar return from the rain is, thus, the sum of the reflectivity of all the drops. As a result, the drop-size distribution is critical to the resultant reflectivity. The variability between most rain clutter

TABLE 5-8 ■ Average Rain Reflectivity versus Frequency Band

		η, dB m^{-1} Transmit frequency, GHz						
Z, dBz	Radar band: Type	S 3.0	C 5.6	X 9.3	K_u 15.0	K_a 35	W 95	mm 140
−12	Heavy stratus clouds				−100	−85	−69	−62
14	Drizzle, 0.25 mm/h	−102	−91	−81	−71	−58	−45*	−50*
23	Light rain, 1 mm/h	−92	−81.5	−72	−62	−49	−43*	−39*
32	Moderate rain, 4 mm/h	−83	−72	−62	−53	−41	−38*	−38*
41	Heavy rain, 16 mm/h	−73	−62	−53	−45	−33	−35*	−37*

* Approximate

Source: From Nathanson [15] (with permission).

models is due to differences in the drop-size distribution selected. Referring to Figure 5-5, recall that the reflectivity of a sphere is a strong function of the ratio of the circumference to the wavelength in the Rayleigh scattering region, so that rain reflectivity depends strongly on the percentage of large drops and will increase with increasing frequency until the resonance region is encountered.

Of course, every rainstorm has a different drop-size distribution, and distributions often change in differing parts of the same storm. Thus, a great deal of variation in the return with both time and space can be expected. Consequently, when discussing average values for reflectivity, it should be understood that considerable variation will be encountered in a realistic situation.

Table 5-8 gives average rain backscatter from several sources for S-band through W-band for several rain situations. As can be seen, the backscatter coefficient increases with increasing frequency (at least up to 35 GHz) and increasing rain rate. Observers of rainstorms have noted that rain drop size increases with increasing rain rate, which accounts for the direct dependence of reflectivity on rain rate. Attenuation has been eliminated from the rain data, so the apparent backscatter can be less for heavy rain rates.[3]

Table 5-8 includes a column listing an alternative scale for rain reflectivity denoted with the symbol Z. This scale, common in meteorological applications, is also called volume reflectivity. It relates radar reflectivity to the distribution of drop sizes, which is more useful for estimating rain rates. It is usually expressed in decibel units and denoted dBz. The relationship between η and Z is [31]

$$\eta = \frac{\pi^5 |K|^2}{\lambda^4} Z \tag{5.28}$$

where K is the complex index of refraction and Z is in units of $m^6/m^3 = m^3$. While K depends on temperature and wavelength, for most weather conditions $|K|^2 \approx 0.93$ for liquid scatterers (e.g., rain, fog) and 0.197 for frozen scatterers (e.g., snow, hail).

For use in meteorology, Z is converted to units of mm^6/m^3 (which requires multiplication of Z in m^3 by 10^{18}) and then to a decibel scale denoted dBz. Thus,

$$Z\ (\text{dBz}) = 10 \log_{10}(10^{18} Z) = 10 \log_{10}(Z) + 180 \tag{5.29}$$

The calculations of equations (5.28) and (5.29) were used to obtain the dBz values in Table 5-8.

[3]Of course, the target echo signal strength is reduced by rain attenuation as well.

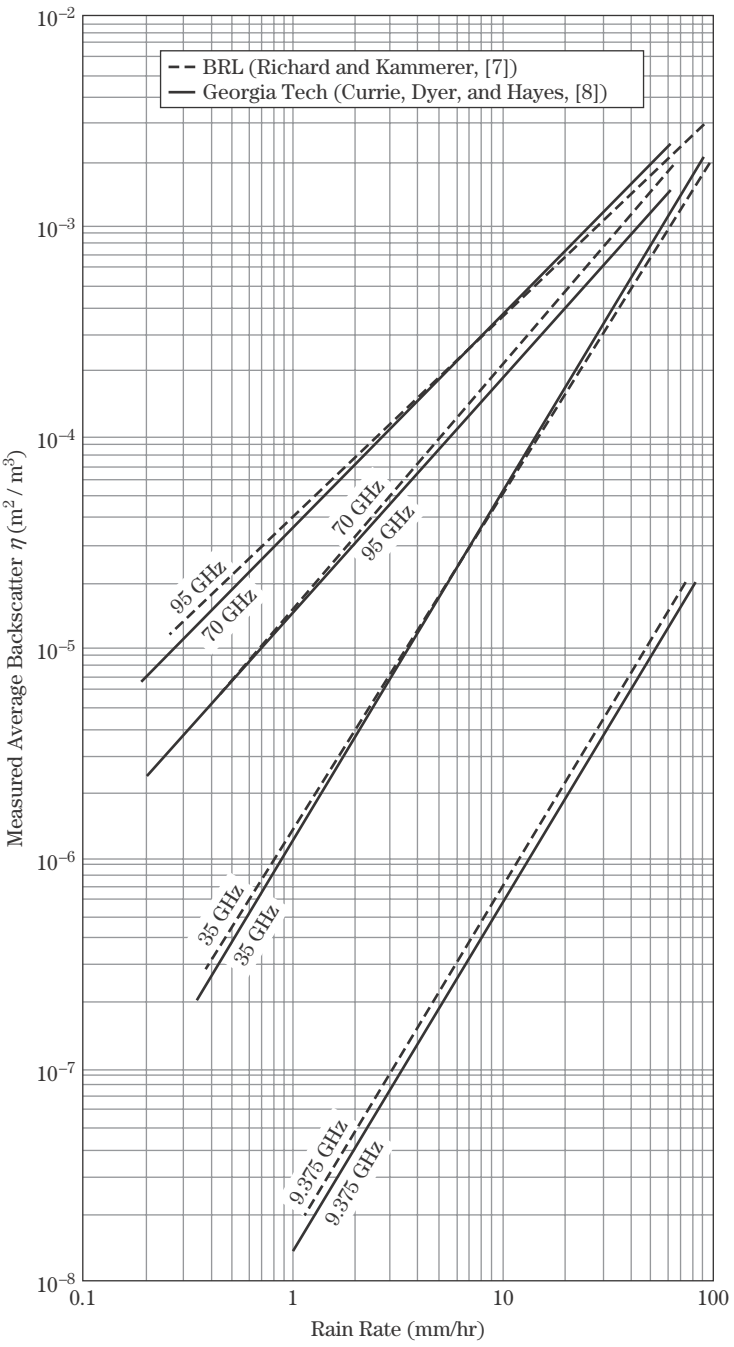

FIGURE 5-33 ■ Least squares fit to rain data at four frequency bands. (From Currie [32]. With permission.)

Figure 5-33 gives least square fit curves to rain data obtained from thunderstorms in a joint experiment between the U.S. Army BRL and GTRI in Orlando, Florida, in the 1970s [32]. Thunderstorms are known for producing large drops, so the wide variation in reflectivity with rain rate is not surprising. One interesting factor is the flattening of the curves at 70 and 95 GHz. This may indicate that the ratio of drop circumference to wavelength is approaching the resonance or optical regions, resulting in a lessened

dependence on drop size. BRL and GTRI each separately analyzed the data, getting slightly different results as shown. However, the overall spread in the data dwarfs these small differences.

Frozen Precipitation As indicated earlier, the reflectivity of frozen precipitation such as snow is generally ignored at microwave frequencies. However, at higher frequencies snow reflectivity can be significant. Figure 5-34 presents data on snow reflectivity at 95,

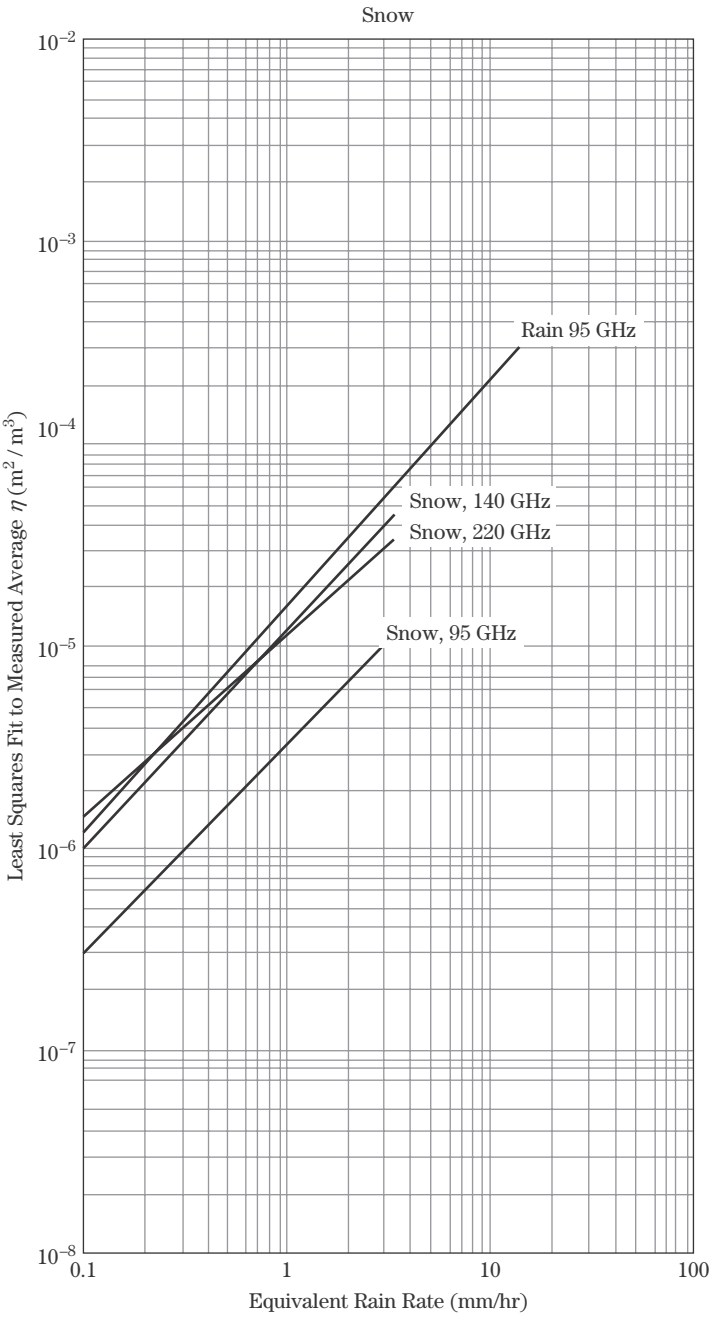

FIGURE 5-34 ■ Least squares fit to snow data at two frequency bands compared with rain data. (From Currie et al. [34]. With permission.)

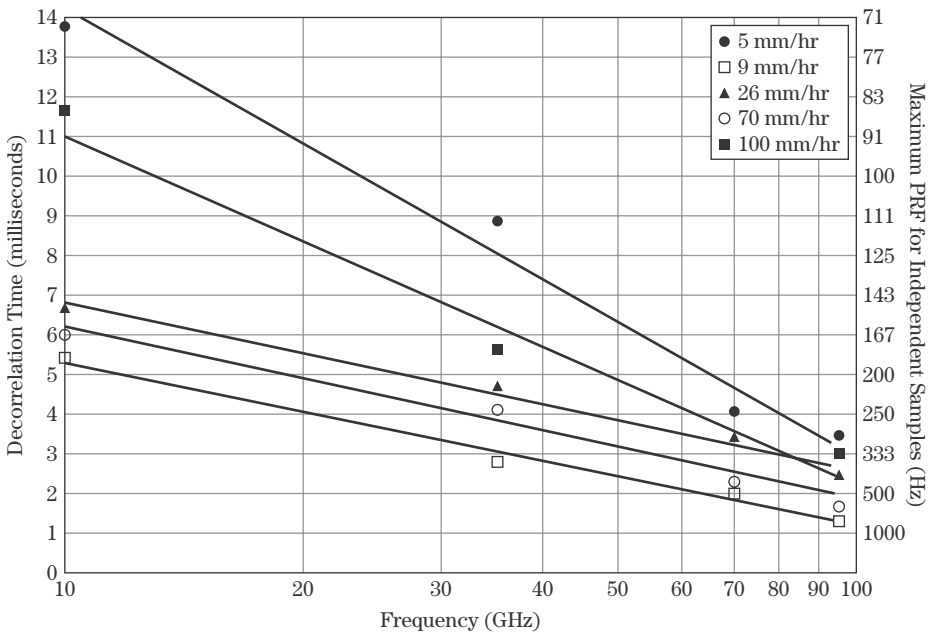

FIGURE 5-35 ■ Decorrelation time for rain backscatter as a function of frequency. (From Currie et al. [8]. With permission.)

140, and 220 GHz measured by Nemarich et al. [33,34] at the U.S. Army Harry Diamond Laboratory compared with the Georgia Tech 95 GHz rain data from Figure 5-33 The snow data are plotted versus equivalent rain rate based on snow water content. While the snow return is much lower at 95 GHz than the rain return, the snow returns at higher frequencies are comparable to the rain return for 95 GHz.

5.2.3.2 Temporal Spectra

Figure 5-35 presents data on the decorrelation time for rain return at 10 through 95 GHz. The maximum PRF for independent samples, calculated as the inverse of the decorrelation time as discussed in Section 5.2.2.4, is given on the right side. Note that for 5 mm/hr rain rate and 10 GHz, the maximum PRF for independent samples is only 71 Hz. At higher rain rates and higher frequencies, the maximum PRF increases significantly.

Figure 5-36 shows the spectral response at 10 through 95 GHz measured during the experiment displayed in Figure 5-33 [35]. Also shown is the Doppler shift for a slow-moving target at 3 mph. The spectral curves were matched to power law functions of the form of equation (5.24) in a manner similar to the data for trees discussed earlier. The figure shows that the rain return frequency spectra would be approximately 15 dB down from the peak (constant power level) at the Doppler frequency for a 3 mph target. This implies that the SCR could be improved by up to 15 dB through the use of careful Doppler processing.

Other important factors related to rain clutter are the spatial extent of a storm (both horizontal and vertical) and its Doppler characteristics, which are affected by prevailing winds, rain rates, and atmospheric turbulence. Attenuation due to rain is extremely important and was discussed in Chapter 4.

5.2.4 Millimeter Wave Clutter

The only difference between millimeter waves and microwaves is the wavelength. However, because of the change in the reflectivity properties of spheres and cylinders as the

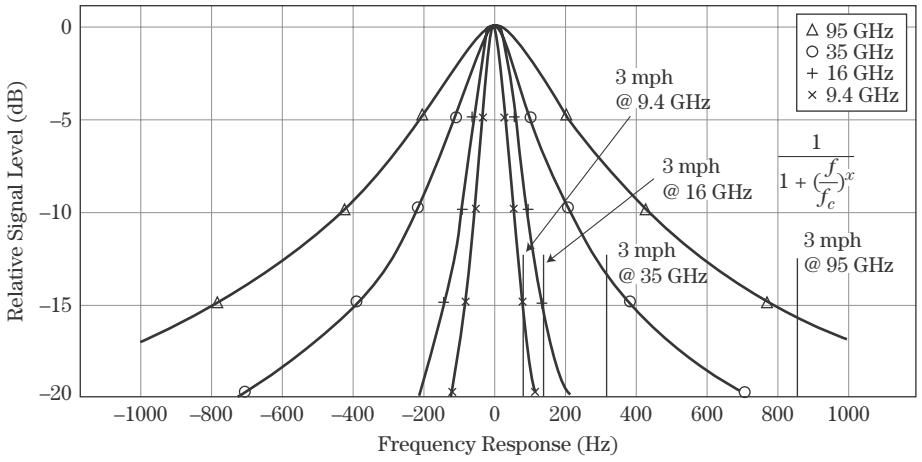

FIGURE 5-36 ■ Rain spectral response for four frequencies compared with a 3 mph moving target. (From Hayes [35]. With permission.)

circumference-to-wavelength ratio approaches unity, significant differences in reflectivity can be observed at higher frequencies. The dependence of rain reflectivity on rain rate at 70 and 95 GHz in Figure 5-33 is one example.

Table 5-9 compares the diameter-to-wavelength ratios of different natural and man-made objects at 35 through 300 GHz. As the ratio approaches 1 or larger unusual reflectivity effects will be observed. From the table it can be seen that this can occur for many types of common scatterers.

As an example of unusual effects at millimeter waves, Figure 5-37 shows the radar reflectivity of snow-covered ground at 35 GHz as a function of time of day. The air temperature was below freezing at the start of the measurement but rose above freezing between 8 a.m. and 8:15 a.m. As can be seen, the reflectivity of the snow dropped about 10 dB in 45 minutes. The temperature continued to hover around freezing, and the reflectivity varied depending on whether the temperature fell below or rose above freezing. This phenomenon has been observed at lower frequencies, but the effect was much smaller. The current theory is that when snow melts and refreezes, large resonant crystals form that reflect RF energy back to the radar, whereas, when melting occurs, surface water prevents

TABLE 5-9 ■ Comparison of the Circumference in Wavelengths of Different Natural and Man-made Items

		Ratio of Diameter to Wavelength (a/λ)			
Scatterer	Diameter (mm)	35 GHz	95 GHz	140 GHz	300 GHz
Raindrops	0.2–6	0.02–0.7	0.6–2	0.09–2.8	0.2–6
Sea Spray	0.2–10	0.02–1.15	0.6–3.3	0.09–4.7	0.2–6
Pine Needles	0.5–1.5	0.057–0.171	0.167–0.5	0.23–0.7	0.5–1.5
Screw Heads	1.5-25	0.17–2.9	0.5–8.3	0.7–11.7	1.5–25
Rivets	10	1.15	3.3	4.7	10
Grass Blades	2–8	0.23–0.92	0.7–2.7	0.93–3.7	2–8
Deciduous Leaves	6–20	0.7–2.31	2.0–6.7	2.8–9.4	6–20
Branches	5–76	0.7–8.78	2.0–25	2.8–35.5	6–76
Snow Crystals	5–50	0.58–5.77	1.7–16	2.3–23.3	5–50
Hail	1–10	0.12–1.15	0.3–3.3	0.47–4.7	1–10

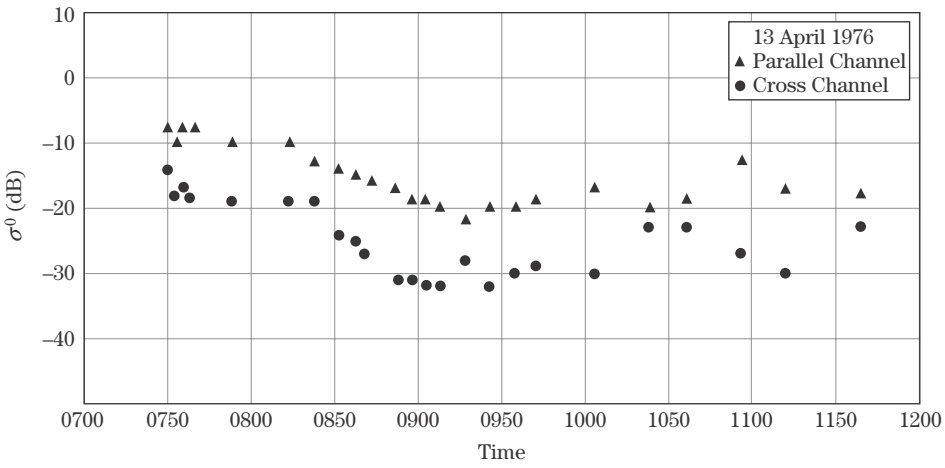

FIGURE 5-37 ■ Snow-covered ground reflectivity at 35 GHz as a function of time of day. (From Currie et al. [36]. With permission.)

penetration into the snow layers to forward scatter more of the energy. The key point of this discussion is that the radar designer must be aware of possible unusual scattering effects as the frequency increases into the millimeter wave region.

5.3 CLUTTER MODELING

5.3.1 General Approaches for Estimating Detection Performance in Clutter

Although a great deal of effort has been expended in developing theoretical models for clutter, most of these models have severe limitations because of the complexity of the real world. As a result, most radar designers either develop their own empirical models from clutter data or use models from the literature to estimate radar performance in clutter. For readers interested in pursuing theoretical modeling, several references are presented at the end of this chapter. The remainder of this section presents some empirical models that have been proven to be of use over the years.

5.3.2 Clutter Models

5.3.2.1 Surface Clutter

In the late 1970's GTRI developed an open literature empirical model for the reflectivity σ^0 of varying types of land clutter for grazing angles in the low angle and plateau regions [36]. In the 1980s this model was extended to higher frequencies, and additional data were used to refine the model [37]. The model takes into account wavelength, rms surface roughness, and grazing angle and has the form

$$\sigma^0 = A(\delta + C)^B \exp\left[\frac{-D}{1 + \dfrac{0.1\sigma_h}{\lambda}}\right] \tag{5.30}$$

TABLE 5-10 ■ Coefficients for GTRI Empirical Model

Constant	Frequency	Soil/ Sand	Grass	Tall Grass Crops	Trees	Urban	Wet Snow	Dry Snow
	3	0.0045	0.0071	0.0071	0.00054	0.362	—	—
	5	0.0096	0.015	0.015	0.0012	0.779	—	—
A	10	0.25	0.023	0.006	0.002	2.0	0.0246	0.195
	15	0.05	0.079	0.079	0.019	2.0	—	—
	35	—	0.125	0.301	0.036	—	0.195	2.45
	95	—	—	—	3.6	—	1.138	3.6
	3	0.83	1.5	1.5	0.64	1.8	—	—
	5	0.83	1.5	1.5	0.64	1.8	—	—
B	10	0.83	1.5	1.5	0.64	1.8	1.7	1.7
	15	0.83	1.5	1.5	0.64	1.8	—	—
	35	—	1.5	1.5	0.64	—	1.7	1.7
	95	—	1.5	1.5	0.64	—	0.83	0.83
	3	0.0013	0.012	0.012	0.002	0.015	—	—
	5	0.0013	0.012	0.012	0.002	0.015	—	—
C	10	0.0013	0.012	0.012	0.002	0.015	0.0016	0.0016
	15	0.0013	0.012	0.012	0.002	0.015	—	—
	35	—	0.012	0.012	0.012	—	0.008	0.0016
	95	—	0.012	0.012	0.012	—	0.008	0.0016
	3	2.3	0.0	0.0	0.0	0.0	—	—
	5	2.3	0.0	0.0	0.0	0.0	—	—
D	10	2.3	0.0	0.0	0.0	0.0	0.0	0.0
	15	2.3	0.0	0.0	0.0	0.0	—	—
	35	—	0.0	0.0	0.0	—	0.0	0.0
	95	—	0.0	0.0	0.0	—	0.0	0.0

Source: From Currie [32] (with permission).

where δ is the grazing angle in radians, σ_h is the rms surface roughness, and A, B, C, and D are empirically derived constants.

Table 5-10 gives the values for A, B, C, and D for frequencies of 3 through 95 GHz for several types of clutter. Figure 5-38 shows the model output for trees at X-band plotted against some GTRI data on tree reflectivity. Note that the model prediction appears a little high when compared to the data since the model attempts to predict an average of both temporal and spatial variations. This model has not been updated to reflect the low angle data reported by Billingsley [11].

Although several empirical models have been developed for sea return, the GTRI model has been one of the more popular ones used, particularly for low angles. The model is based on many years of radar data collection at a test site near Boca Raton, Florida. The model predicts average sea clutter values as a function of polarization, wavelength, grazing angle, radar boresight-wind direction, average wave height, and wind speed. Table 5-11 summarizes the equations for the model.

The definitions of variables are as follows:

- λ is the radar wavelength.
- δ is the grazing angle.

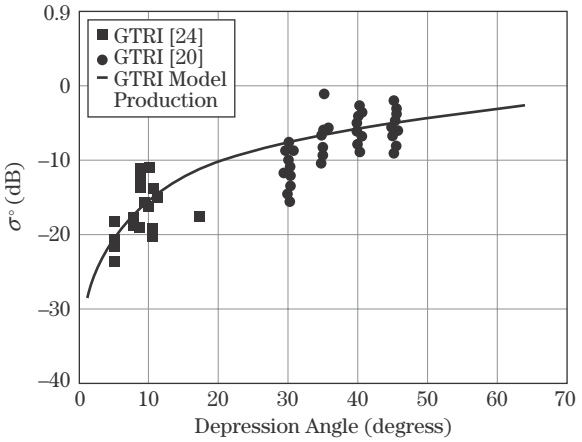

FIGURE 5-38 ■ Comparison of GTRI model output with data for deciduous trees at X-band. (From Currie [32]. With permission.)

- ϕ is the angle between radar boresight and wind direction.
- h_{av} is the average wave height.
- A_i is the "interference factor," which takes into account rms surface roughness and multipath.
- A_u is the upwind/downwind factor.
- A_w is the wind speed factor.

Figure 5-39 gives a sample output of the model. Shown is the value of σ^0 as a function of bore sight-upwind direction for three frequencies. (The model assumes that the wind and waves are proceeding in the same direction.) Note that after the original 1 to 10 GHz sea clutter model was developed, a second model was developed for 10 to 100 GHz [38].

TABLE 5-11 ■ GTRI Sea Clutter Model Equations

$\sigma^0_{HH} = 10\log[3.9 \times 10^{-6}\lambda\delta^{0.4}A_i A_u A_w]$
For 1 to 3 GHz $\sigma^0_{VV} = \sigma^0_{HH} - 1.73\ln(h_{av} + 0.015) + 3.76\ln(\lambda) + 2.46\ln(\delta + 0.0001) + 222$
For 3 to 10 GHz $\sigma^0_{VV} = \sigma^0_{HH} - 1.05\ln(h_{av} + 0.015) + 1.09\ln(\lambda) + 1.27\ln(\delta + 0.0001) + 9.70$
$\sigma_\phi = (14.4\lambda + 5.5)\delta h_{av}/\lambda$
$A_i = \sigma_\phi^4\left(1 + \sigma_\phi^4\right)$
$A_u = \exp\left[0.2\cos\phi(1 - 2.8\delta)(\lambda + 0.015)^{-0.4}\right]$
$qw = 1.1/(\lambda + 0.015)^{-0.4}$
$V_w = 8.67h_{av}^{0.4}$
$A_w = [1.94V_w/(1 + V_w/15.4)]^{qw}$

Note: Values for h_{av} and λ are given in meters, δ and ϕ are in radians.
Source: From Horst et al. [39] (with permission).

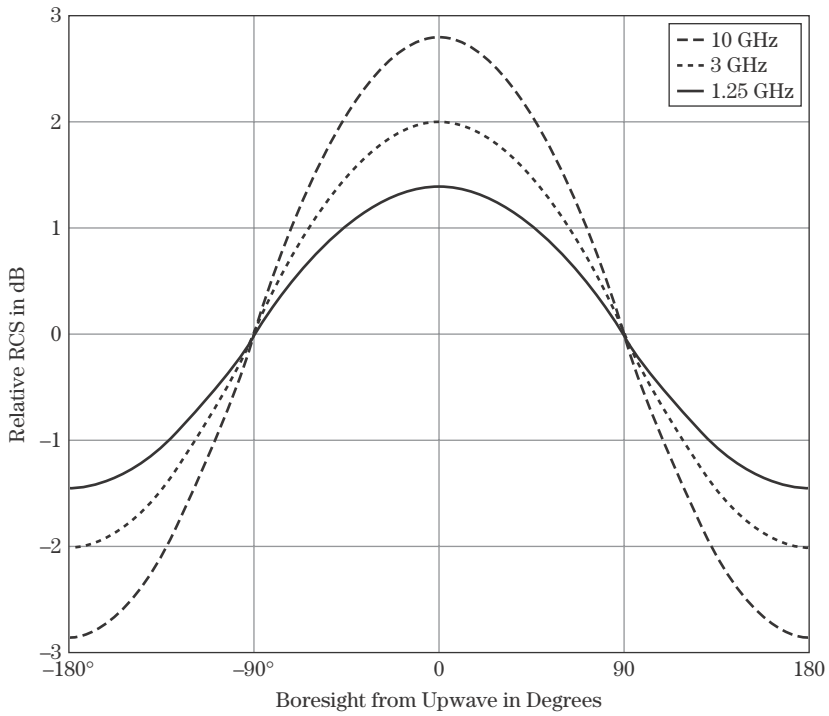

FIGURE 5-39 ■ GTRI sea clutter model output for three frequencies at 1° grazing angle. (From Long [6]. With permission.)

Unfortunately, the experimenters used a different X-band data set from that used for the original model development so that the results of the two models do not agree at 10 GHz. Some users that need to model sea return over the entire frequency range average the results from the two models at 10 GHz.

5.3.2.2 Atmospheric Clutter Models

The equations for the least squares fit to rain data presented in Figure 5-33 are presented in Table 5-12. The equations have the form

$$\eta = AR^B \text{ m}^{-1} \tag{5.31}$$

where η is the radar cross section per unit volume, and A and B are constants given in Table 5-12. Note that significant variability in the data occurred around the calculated least squares fits.

TABLE 5-12 ■ Model Coefficients for Rain

Frequency (GHz)	A	B
9.4	1.3×10^{-8}	1.6
35	1.2×10^{-6}	1.6
70	4.2×10^{-5}	1.1
95	1.5×10^{-5}	1.0

Source: From Currie et al. [34] (with permission).

5.4 CONCLUDING REMARKS

This chapter defined the required terminology for dealing with radar clutter; discussed the average, temporal, and spatial properties of clutter; and introduced some empirical models for clutter. In no way should this discussion be considered as comprehensive in nature. Dozens of books have been written on this topic from both theoretical and empirical points of view. Some of these books are listed in Section 5.5. The next section provides a summary of average clutter data taken from the sources discussed previously.

5.4.1 Reflectivity Summary

Table 5-13 gives some average values for land clutter as a function of aspect angle that are plotted in Figures 5-11 through 5-14, which were adapted from Nathanson [15]. Table 5-14 summarizes average values for sea clutter as a function of polarization and depression angle which were plotted in Figures 5-18 through 5-20, again adapted from Nathanson. These data reflect the general trends discussed previously but omit any dependence on wind direction, a weakness corrected by the GTRI model of Table 5-11.

Table 5-8 given previously summarizes average values for rain return as a function of frequency and rain rate, again, taken from Nathanson [15].

The temporal and spatial variations of land clutter were best represented by Weibull distributions. The width parameters (standard deviation or Weibull width parameter) for land clutter were given in Tables 5-4 and 5-7. Spectral bandwidth and roll-off characteristics for wind-blown trees were presented in Table 5-6. Rain spectral constants were presented in Figure 5-35.

TABLE 5-13 ■ Summary of Averaged Land Reflectivity (σ^0 in db)

		Grazing Angle (Deg.)			
Clutter Type	Frequency Band	1.5	10	30	60
Desert	L	−45	−38	−28	−21
	S	−46	−36	−25	−17
	C	−40	−33	−23	−16
	X	−40	−30	−21	−14
	K_u		−28	−19	−13
Farmland	L	−36	−30	−20	−15
	S	−34	−28	−18	−16
	C	−33	−26	−16	−15
	X	−33	−26	−16	−14
	K_u	−23	−22	−16	−13
Woods	L	−28	−26	−18	−19
	S	−28	−24	−16	−15
	C	−27	−23	−16	−15
	X	−26	−23	−14	−14
	K_u	−13	−20	−14	−12
Urban	L	−25	−18	−15	−12
	S	−23	−18	−13	−11
	C	−21	−18	−11	−10
	X	−20	−16	−10	−10
	K_u				

TABLE 5-14 ■ Summary of Averaged Sea Reflectivity (σ^0 in db)

Sea State	Frequency Band	Polarization	Grazing Angle (Deg.) 0.1	10	30	60
1	L	VV		−39	−38	−22
	L	HH		−56	−46	−24
	S	VV	−80	−40	−40	−24
	S	HH	−80			−25
	C	VV	−72	−41	−42	−24
	C	HH	−75	−53	−48	−26
	X	VV	−65	−42	−36	−24
	X	HH	−71	−51	−44	−24
	K_u	VV		−40	−31	−20
	K_u	HH			−38	−20
3	L	VV	−82	−34	−30	−18
	L	HH	−82	−48	−39	−20
	S	VV	−75	−34	−29	−19
	S	HH	−68	−46	−38	−20
	C	VV	−60	−34	−28	−18
	C	HH	−69	−40	−37	−20
	X	VV	−51	−32	−26	−16
	X	HH	−53	−37	−34	−21
	K_u	VV		−31	−23	−14
	K_u	HH		−32	−28	−16

5.4.2 Clutter Effect on Detection

This chapter has summarized the clutter characteristics and provided clutter data and modeling for simulating clutter. Clutter limits detection of targets due to its competing signal, which interferes with the target signal. Methods for dealing with these problems using Doppler processing are discussed in Chapter 17.

5.5 FURTHER READING

Perhaps the two best comprehensive references for understanding radar clutter are the texts by Long [6] and Ulaby and Dobson [10]. Both combine in-depth discussion of clutter phenomenology and modeling with extensive summaries of real-world clutter measurements. Ward et al. concentrate on sea clutter measurements and modeling with the K-distribution in [25].

More extensive theoretical analyses are given for sea clutter by Ward et al. in [25] and for various clutter sources in [40–43]. An in-depth analysis of land clutter data is given by Billingsley [11]. Other good reviews of land and sea clutter data can be found in [15,40–43].

Most of the preceding sources are concerned with radar clutter at microwave frequencies. Additional discussion of millimeter-wave clutter data is available in the publications by Currie and various colleagues [34,44,45].

5.6 REFERENCES

[1] Novak, L.M., and Owirka, G.J., "Radar Target Identification Using an Eigen-Image approach," *1994 IEEE National Radar Conference*, Atlanta, GA, p. 130, March 29–31, 1994.

[2] Long, M.W., "Radar Clutter," Tutorial presented at the *2006 IEEE Radar Conference,* Verona, NY, April 2006.

[3] Mott, H., *Polarization in Antennas and Radar*, Wiley, New York, 1986.

[4] Holm, W.A., "MMW Radar Signal Processing Techniques," Chapter 6 (pp. 279–310) in *Principles and Applications of Millimeter-Wave Radar*, Ed. N.C. Currie and C.E. Brown, Artech House, Norwood, MA, 1987.

[5] Echard, J.D., et al., "Discrimination between Targets and Clutter by Radar," Final Technical Report on Contract DAAAG-29-780-C_0044, Georgia Tech Research Institute, Atlanta, December 1981.

[6] Long, M.W., *Radar Reflectivity of Land and Sea*, 3d ed., Artech House, Norwood, MA, 2001.

[7] Richard, V.W., and Kammerer, J.E., "Rain Backscatter Measurements and Theory at Millimeter Wave Measurements," Report No. 1838, U.S. Army Ballistic Research Laboratory, Aberdeen Proving Ground, MD, October 1975.

[8] Currie, N.C., Dyer, F.B., and Hayes, R.D., "Analysis of Radar Rain Return at Frequencies of 9.375, 35, 70, and 95 GHz," Technical Report No. 2 on Contract DAAA 25-76-C-0256, Georgia Tech Research Institute, Atlanta, February 1975.

[9] Nemarich, J., Wellman, R.J., and Lacombe, J., "Backscatter and attenuation of Falling Snow and Rain at 96, 140, and 220 GHz," *IEEE Trans. Geoscience and Remote Sensing*, vol. 26, no. 3, pp. 330–342, May 1988.

[10] Ulaby, F.T., and Dobson, M.C., *Handbook of Radar Scattering statistics for Terrain,* Artech House, Norwood, MA, 1989.

[11] Billingsley, J.B., *Low-Angle Radar Land Clutter*, William Andrew Publishing, Norwich, NY, 2002.

[12] Aley, J.C., Davis, W.T., and Mills, N.B., "Radar Sea Return in High Sea States," Naval Research Laboratory Report No. 7142, September 1970.

[13] Long, M.W., et al., "Wavelength Dependence of Sea Echo," Final Report on Contract N62269-3019, Georgia Tech Research Institute, Atlanta, 1965.

[14] Trebits, R.N., et al., "Millimeter Wave Radar Sea Return Study," Interim Technical Report on Contract N60921-77-C-A168, Georgia Tech Research institute, Atlanta, July 1978.

[15] Nathanson, F.E., "Sea and Land Backscatter," Chapter 7 in *Radar Design Principles,* 2d ed., McGraw-Hill, Inc New York, 1991.

[16] Currie, N.C., "Performance Tests on the AN/TPQ-31a Radar," Technical Report on Contract N00014-75-C-0228, Mod P00001, Georgia Tech Research Institute, Atlanta, 1975.

[17] "Radar Return Study," Goodyear Aircraft Corp., Final Report on Contract NOAS-59-6186-CGERA 463, Phoenix, AZ, September 1959.

[18] Stiles, W.H., Ulaby, F.T., and Wilson, E., "Backscatter Response of Roads and Roadside Surfaces," Sandia Report No. SAND78-7069, University of Kansas center for Research, Lawrence, March 1979.

[19] Dyer, F.B., and Currie, N.C., "Some Comments on the Characteristics of Radar Sea Echo," 1974 IEEE APS International Symposium, Atlanta, GA, June 1974, pp. 323–326.

[20] Rivers, W.K., "Low Angle Sea Return at 3mm Wavelength," Final Technical Report on Contract N62269-70-C-0489, Georgia Tech Research Institute, Atlanta, November 1970.

[21] Currie, N.C., Dyer, F.B., and Hayes, R.D., "Radar Land Clutter Measurements at 9.375, 16, 35, and 95 GHz," Technical Report No. 3 on Contract DAA25-73-0256, Georgia Tech Research Institute, Atlanta, February 1975.

[22] Fishbein, W., et al., "Clutter Attenuation Analysis," Technical Report No. ECOM-2808, US Army ECOM, Ft, Monmouth, NJ, March 1967.

[23] Simpkins, W.L., Vannicola, V.C., and Ryan, J.P., "Seek Igloo Radar Clutter Study," Technical Report No. RADC-TR-77-338, RADC, Rome, NY, October 1977.

[24] Booth, R.R., "The Weibull Distribution Applied to Ground Clutter Backscatter Coefficient," Report No. RE-TR-69-15, US Army Missile command, Huntsville, AL, June 1969.

[25] Ward, K.D., Tough, R.J.A., and Watts, S., *Sea Clutter: Scattering, the K Distribution and Radar Performance*, Institution of Engineering and Technology, London, 2006.

[26] Ward, K.D., "Compound Representation of High Resolution Sea Clutter," *Electron Lett*., vol. 17, pp. 561–565, 1981.

[27] Watts, S., "Radar Detection Prediction in K-Distributed Sea Clutter and Thermal Noise," *IEEE Trans. AES*, vol. 23, pp. 40–45, 1987.

[28] Walker, D., "Doppler Modelling of Radar Sea Clutter," *IEE Proceedings—Radar, Sonar and Navigation,* vol. 148, no. 2, pp. 73–80, April 2001.

[29] Plummer, D.K., et al., "Some Measured Statistics of Coherent Radar Sea Echo and Doppler at L-Band," Final Technical Report on Contract NADc-78254-30, Georgia Tech Research Institute, Atlanta, December 1969.

[30] Werle, B.O., "Sea Backscatter Spikes, and Wave Group Observations at Low Grazing Angles," *Proceedings of the 1995 IEEE International Radar Conference*, Washington, DC, pp. 187–195, May 1995.

[31] Richards, M.A., *Fundamentals of Radar Signal Processing*, McGraw-Hill, New York, 2005.

[32] Currie, N.C., "MMW Clutter Characteristics," Chapter 5 in *Principles and Applications of Millimeter-Wave Radar*, Ed. N.C. Currie and C.E. Brown, Artech House, Norwood, MA, 1987.

[33] Nemarich, J., et al., "Comparative Near Millimeter Wave Propagation Properties of Snow and Rain," *Proceedings of Snow Symposium III*, U.S. Army CRREL, Hanover, NH, August 1983.

[34] Currie, N.C., Hayes, R.D., and Trebits, R.N., *Millimeter-Wave Radar Clutter*, Artech House, Norwood, MA, 1992.

[35] Hayes, R.D., private communication, Atlanta, GA, 1980.

[36] Currie, N.C., et al., "Radar Millimeter Wave Measurements: Part 1, Snow and Vegetation," Report No. AFATL-TR-77-92, July 1977.

[37] Currie, N.C., and Zehner, S.P., "MMW Land clutter Model," *IEE Radar 82 International Symposium*, London, September 1982.

[38] Horst, M.M., and Perry, B., "MMW Modeling Techniques," Chapter 8 in *Principles and Application of Millimeter-Wave Radar*, Ed. N.C. Currie and C.E. Brown, Artech House, Norwood, MA, 1987.

[39] Horst, M.M., Dyer, F.B., and Tuley, M.T., "Radar Sea Clutter Model," Proceedings of the IEEE Conference on Antennas and Propagation, November 1978.

[40] Skolnik, M.I., *Radar Handbook,* 2d ed., Chapters 12, "Ground Echo" and 13, "Sea Echo," McGraw-Hill Publishing Company, New York, 1990.

[41] Ulaby, F.T., Moore, R.K., and Fung, A.K., *Microwave Remote Sensing: Vol. II, Radar Remote Sensing and Surface Scattering and Emission Theory*, Addison-Wesley Publishing Company, Reading, MA, 1982.

[42] Ulaby, F.T., and Elachi, C. (Eds.), *Radar Polarimetry for Geoscience Applications*, Artech House, Norwood, MA, 1990.

[43] Bogush Jr., A.G., *Radar and the Atmosphere*, Artech House, Norwood, MA, 1989.

[44] Currie, N.C., and Brown, C.E. (Eds.), "MMW Clutter Characteristics," Chapter 5 in *Principles and Applications of Millimeter-Wave Radar*, Artech House, Norwood, MA, 1987.

[45] Button, K.J., and Wiltse, J.C. (Eds.), "Millimeter Radar," Chapter 2 in *Infrared and Millimeter Waves: vol. 4, Millimeter Systems*, Academic Press, New York, 1981.

5.7 PROBLEMS

1. A radar has a pulse length of $\tau = 10$ μs, an azimuth beamwidth $\theta_3 = 3^\circ$, and an elevation beamwidth $\phi_3 = 3^\circ$. At what grazing angle δ does the transition occur between the pulse-limited and beam-limited ground clutter cases when the nominal range to the ground is $R = 10$ km? Repeat for $R = 50$ km.

2. For the same radar used in problem 1, what is the volume V in cubic meters of a volume clutter resolution cell at $R = 10$ km? Repeat for $R = 50$ km.

3. A radar is attempting to detect a point target in the presence of ground clutter. The parameters of the radar and its environment are such that the SNR at a range of $R_0 = 10$ km is 30 dB, while the SCR at the same range is 20 dB. The detection performance at this range is "clutter limited" because the clutter is the dominant interference. Assume the clutter interference is pulse-limited and that σ^0 does not vary with range. At what range will the SNR and SCR be equal? (At ranges longer than this, the detection performance for this target will be "noise limited.")

4. Consider two radar targets with polarization scattering matrices $\mathbf{S}_1$ and $\mathbf{S}_2$ as follows:

$$\mathbf{S}_1 = \begin{bmatrix} 1 & 0 \\ 0 & 1 \end{bmatrix}, \quad \mathbf{S}_2 = \begin{bmatrix} 1 & j \\ -j & -1 \end{bmatrix}$$

where $j = \sqrt{-1}$. Compute the parallel/cross-polarization ratio and the vertical/horizontal polarization ratio for each target. Which ratio could be used to discriminate between the two targets?

5. Compute the critical grazing angle for an X-band (10 GHz) radar when the surface roughness σ_h is 1.0 cm, and again when $\sigma_h = 10.0$ cm. Repeat for an L-band (1 GHz) radar and a K-band (35 GHz) radar.

6. Compute the diameter of a conducting sphere at the boundary between the Rayleigh and resonance regions at a radar frequency of 5 GHz (C-band). Repeat for the boundary between the resonance and optics regions.

7. Show that the Weibull distribution reduces to the exponential distribution when $b = 1$, and to the Rayleigh distribution when $b = 2$.

8. A radar collects $N_t = 30$ samples of clutter data having a decorrelation time τ_0 of 200 μs. What is the number of uncorrelated samples N_i if the PRF is 1 kHz? Repeat for PRF = 5 kHz and 40 kHz.

9. Consider the GTRI model for land clutter reflectivity given by equation (5.30). Show that the model predicts that σ^0 becomes independent of surface roughness when $\sigma_h \ll 10\lambda$.

10. Use equations (5.28) and (5.29) to confirm that a reflectivity $\eta = -92$ dB corresponds to a meteorological reflectivity of 23 dBz at S-band (3 GHz) as shown in Table 5-8.